inorganics

MDPI

Article

Ligand Rigidity and π-Surface Modulate Biomolecular Interactions and Cytotoxicity in Ru(II) Polypyridyl Complexes

Patrícia Alves de Matos [1], Marcos Eduardo Gomes do Carmo [1], André Luis Araújo Parussulo [2], Clara Maria Faria Silva [3], Ricardo Campos Lino [3], Henrique Eisi Toma [2], Marcelo Emílio Beletti [4], Robson José de Oliveira Júnior [3], Antônio Otávio de Toledo Patrocinio [1], Tiago Araújo Matias [5,*] and Tayana Mazin Tsubone [1,*]

1 Institute of Chemistry, Federal University of Uberlândia (UFU), Uberlândia 38408-100, MG, Brazil; patricia.matos@ufu.br (P.A.d.M.); marcos.go.carmo@gmail.com (M.E.G.d.C.); otaviopatrocinio@ufu.br (A.O.d.T.P.)
2 Institute of Chemistry, University of São Paulo (USP), São Paulo 05508-900, SP, Brazil; henetoma@iq.usp.br (H.E.T.)
3 Institute of Biotechnology, Federal University of Uberlândia (UFU), Uberlândia 38402-045, MG, Brazil; clara.faria@ufu.br (C.M.F.S.); ricardo.lino@ufu.br (R.C.L.); oliveirajunior@ufu.br (R.J.d.O.J.)
4 Institute of Biomedical Sciences, Federal University of Uberlândia (UFU), Uberlândia 38408-100, MG, Brazil; mebeletti@ufu.br
5 Chemistry Department, Federal University of Espírito Santo (UFES), Vitória 29075-910, ES, Brazil
* Correspondence: tiago.matias@ufes.br (T.A.M.); tayana.tsubone@ufu.br (T.M.T.)

Abstract

The complexes *cis*-[Ru(dmbpy)$_2$Cl(bpy)](PF$_6$) (Rubpy) and *cis*-[Ru(dmbpy)$_2$Cl(bpe)](PF$_6$) (Rubpe) (dmbpy = 4,4′-Dimethyl-2,2′-dipyridyl, bpy= 4,4′-dipyridyl and bpe = 1,2-bis(4-pyridyl)ethane) were synthesized and spectroelectrochemically characterized. Both Ru(II) complexes exhibited absorption bands assigned to intraligand and metal-to-ligand charge transfer (MLCT) transitions, and their spectral stability in PBS buffer (pH 7.4) supports their suitability for biological studies involving biomolecules or living cells. Fluorescence quenching assays revealed strong interactions with bovine serum albumin (BSA), with binding constants (K_b) values were 2.89 × 10^5 M^{-1} for Rubpy and 1.97 × 10^5 M^{-1} for Rubpe, and a stoichiometry of one binding site per albumin molecule. DNA-binding studies demonstrated non-covalent interactions with ss-DNA, evidenced by a hyperchromic effect in the MLCT bands, suggesting a partial intercalation or groove-binding mechanism. Cellular uptake assays indicated moderate incorporation of both complexes in tumor cells, with uptake levels of 52% (Rubpy) and 47% (Rubpe) in HeLa cells, and 42% (Rubpy) and 32% (Rubpe) in MDA-MB-231 cells. Despite the similar uptake profiles, cytotoxicity assays showed that Rubpe is approximately 2.4 times more potent than Rubpy, with IC_{50} values of 9 μM (HeLa) and 12 μM (MDA-MB-231), compared to 22 μM and 29 μM for Rubpy, respectively. These results highlight the relevance of these Ru(II) complexes as molecular platforms for exploring structure–activity relationships in anticancer agents.

Keywords: ruthenium(II) polypyridine; albumin (BSA); cellular toxicity; biomolecule interaction

Check for updates

Academic Editor: Dušan Dimić

Received: 23 November 2025
Revised: 19 December 2025
Accepted: 23 December 2025
Published: 19 February 2026

Copyright: © 2026 by the authors. Licensee MDPI, Basel, Switzerland. This article is an open access article distributed under the terms and conditions of the Creative Commons Attribution (CC BY) license.

1. Introduction

Although platinum(II)-based anticancer compounds have achieved significant success in clinical oncology, their prolonged use is often associated with severe limitations, including increased drug efflux, reduced cellular uptake, rapid DNA repair, and poor tumor

selectivity, ultimately contributing to drug resistance [1]. As alternatives, ruthenium-based complexes have been identified as promising candidates due to their distinct chemical properties and biological behavior [2]. In particular, Ru(II) polypyridine complexes have attracted considerable attention because of their lower toxicity, slower ligand dissociation, reduced resistance development, strong interactions with biomacromolecules, and cytotoxic activity in various cancer models [2–5]. Several Ru-based agents have progressed to clinical evaluation, including the Ru(III) compounds NAMI-A and KP1019/KP1339, and the Ru(II) phototherapeutic TLD1433 [2]. While NAMI-A showed limited efficacy in phase II trials, KP1019's solubility issues were overcome in its sodium derivative BOLD-100, which has demonstrated clinical activity and is currently in global phase II trials for gastrointestinal cancers [6,7]. Meanwhile, TLD1433 advanced to phase II investigations for the photodynamic treatment of bladder cancer [8].

The antitumor properties of Ru(II) complexes are highly dependent on ligand design, coordination geometry, and the presence of labile sites within the metal center. Subtle modifications in ligand electronics or sterics can significantly alter DNA and protein interactions [9]. For example, complexes of the type $[Ru(R\text{-}tpy)(LL)Cl]^{n+}$ (R = Chloro or 4-chlorophenyl; LL = bidentate ligand) exhibit strong cytotoxic activity against multiple tumor cell lines, where the aromaticity of the terpyridine substituent has been shown to enhance biological activity [9–11]. Similar trends have been observed for mixed-ligand complexes such as $[Ru(ppy)(phen)(NCCH_3)_2]^+$ and $[Ru(bpy)(ppy)(dppz)]^+$, whose hydrophobic ligands facilitate rapid cellular uptake and nuclear accumulation [12]. Overall, Ru(II) polypyridyl complexes containing hydrophobic bidentate ligands such as bpy, phen, or derivatives often display higher cytotoxicity due to enhanced membrane permeability and intracellular accumulation [5,9,12,13].

The biological activity of ruthenium complexes is influenced not only by interactions with DNA but also by their ability to bind proteins [14,15]. Protein binding plays a central role in drug pharmacokinetics and distribution, and regulatory agencies such as the FDA require early-stage evaluation of protein interactions during drug development [16]. Serum albumin, which is highly abundant in plasma, is particularly important because it modulates drug transport, bioavailability, and accumulation in tumor tissues [2]. Consequently, BSA is commonly used as a model for studying protein binding and its implications for cytotoxicitys [14].

Inspired by the relevance of ligand-controlled structure–activity relationships in Ru(II) polypyridyl scaffolds, we examined two complexes differing only in their ancillary ligands (Figure 1) as potential antitumor candidates: *cis*-$[Ru(dmbpy)_2Cl(bpy)](PF_6)$ (or Rubpy) and *cis*-$[Ru(dmbpy)_2Cl(bpe)](PF_6)$ (or Rubpe) (dmbpy = 4,4′-Dimethyl-2,2′-bipyridyl, bpy = 4,4′-bipyridyl and bpe = 1,2-bis(4-pyridyl)ethane)). Although Ru(II) polypyridyl complexes have been widely studied, direct comparisons that isolate the influence of ligand rigidity and π-surface, such as the rigid, fully conjugated bpy versus the flexible, reduced-π bpe, remain limited. These ligands provide a minimal and well-defined structural variation, enabling a controlled assessment of how such differences affect biomolecular interactions and cellular responses. From a structure–property perspective, bpy offers a rigid π-conjugated platform that favors π-stacking with nucleic acids, whereas bpe provides greater conformational freedom and a reduced aromatic surface, features that may influence hydrophobic partition, membrane interactions, and intracellular reorganization. This framework establishes the rationale for interpreting the distinct biomolecular and cytotoxic behaviors observed for Rubpy and Rubpe.

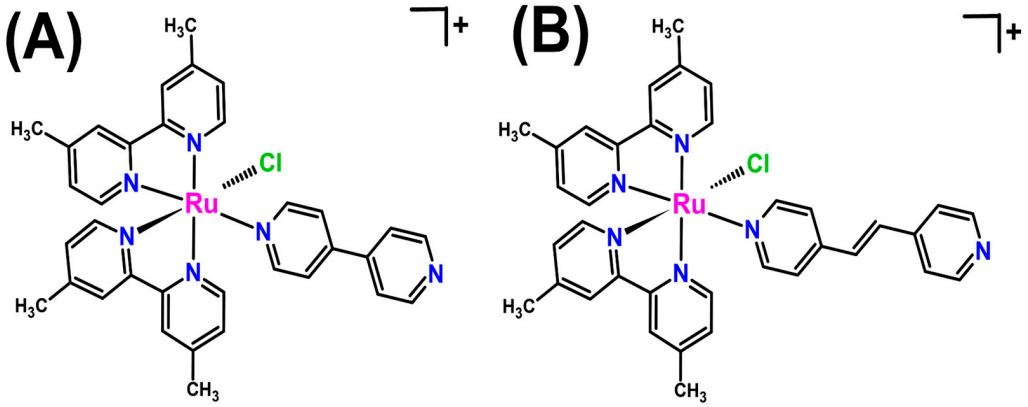


Figure 1. Chemical structures of studied Ru(II) complexes. (**A**) *cis*-[Ru(dmbpy)$_2$Cl(bpy)](PF$_6$) (or Rubpy) and (**B**) *cis*-[Ru(dmbpy)$_2$Cl(bpe)](PF$_6$) (or Rubpe). dmbpy = 4,4′-Dimethyl-2,2′-bipyridyl, bpy = 4,4′-dipyridyl and bpe = 1,2-bis(4-pyridyl)ethane.

2. Results and Discussion

2.1. Characterization and Physicochemical Properties

2.1.1. Electronic Structure and Redox Properties of the Ru(II) Complexes

To gain insight into the physicochemical behavior of Rubpy and Rubpe and to ensure the integrity of the species investigated in biomolecular and cellular assays, we first examined their electronic, redox, and spectroelectrochemical properties, as well as their stability under aqueous and physiological conditions.

Both complexes display the characteristic absorption profile of Ru(II) polypyridyl scaffolds (Figure 2A), with intense intraligand $\pi \rightarrow \pi^*$ transitions near 292 nm and broad metal-to-ligand charge transfer (MLCT) bands centered around 400–460 nm. These features arise from Ru(II)$\rightarrow\pi^*$ transitions involving the coordinated polypyridyl ligands and are fully consistent with previously reported Ru(II) complexes of similar composition [17]. The electrochemical behavior also follows the expected pattern for this family of compounds: cyclic voltammograms reveal a reversible Ru(III)/Ru(II) oxidation at $E_{1/2} \approx 0.81$–0.83 V, followed by two ligand-centered reductions at negative potentials (Figure 2B). These reductive processes, observed at −1.38 and −1.57 V for Rubpy and at −1.29 and −1.50 V for Rubpe, correspond to successive one-electron reductions in the bipyridyl-type ancillary ligands ($L^{0/-}$ and $L^{-/2-}$ for L = bpy or bpe), in agreement with literature data [17].

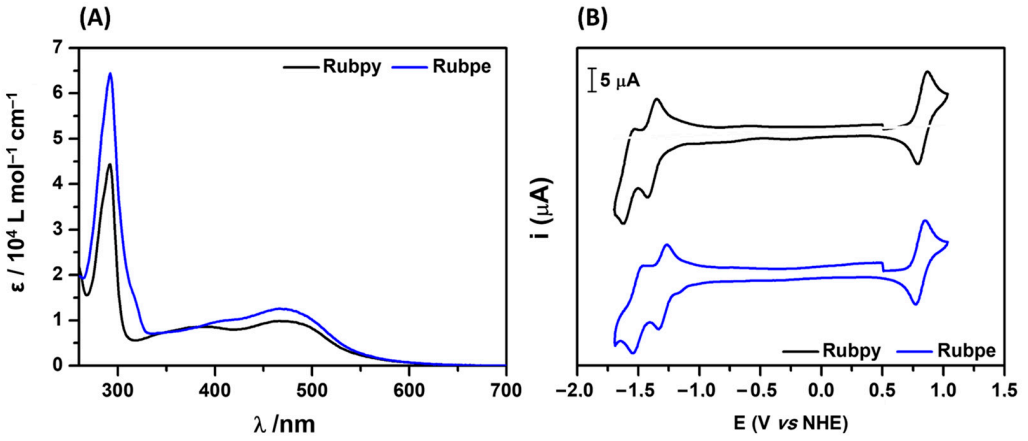


Figure 2. (**A**) Electronic absorption spectra of Rubpy and Rubpe complexes in methanol solution. (**B**) Cyclic voltammograms of Rubpy and Rubpe complexes in 1.0 mM of (Bu_4N)(ClO_4) in DMF, at scan rate of 100 mVs^{-1}.

Spectroelectrochemical measurements (Figures S1–S3) further corroborate these assignments. Oxidation of the ruthenium center results in the extinction of the MLCT bands between 383 and 530 nm and a decrease in the ligand-centered π→π* transition near 292 nm (Figure S1A). Upon electrochemical reduction in *cis*-[Ru^{III}(dmbpy)$_2$Cl(bpy)]$^{2+}$ back to the Ru(II) form, the MLCT bands at 383 and 470 nm reappear, together with the restored π→π* band (Figure S2A). Such reversibility is typical of inert Ru(II) complexes of the type *cis*-[Ru(bpy)L(py)]$^{n+}$, which are well known for their high stability and use in various catalytic applications [18].

Reduction of the bpy or bpe ancillary ligand induces a characteristic decrease in the intraligand absorption near 300 nm, accompanied by an increase in absorbance above 348 nm and a bathochromic shift in the MLCT bands (Figures S1B and S3B). A similar pattern is observed in the second ligand-centered reduction (Figures S1C and S3C), with further enhancement of low-energy transitions and attenuation of the π→π* band [17]. The close structural similarity between Rubpy and Rubpe results in nearly identical spectroelectrochemical profiles, with comparable redox potentials and analogous spectral changes upon oxidation and reduction.

Notably, no redox processes were detected in the potential window between −0.24 and −0.15 V, a range associated with the intracellular redox state of proliferating (−0.24 V), apoptotic (−0.17 V), and necrotic cells (−0.15 V) [19]. The absence of redox activity in this biologically relevant region suggests that both complexes are electrochemically stable under typical cellular redox environments.

2.1.2. Stability of the Complexes in Aqueous and Physiological Media

Water constitutes approximately 70% of the cellular environment and acts as the primary solvent for physiological buffer systems such as phosphate-buffered saline (PBS). Under these conditions, water molecules (H_2O) and phosphate species (HPO_4^{2-}/$H_2PO_4^-$) may function as Lewis bases capable of coordinating to metal centers. Chloro-ruthenium polypyridyl complexes can undergo ligand substitution reactions in aqueous media, forming aqua species through chloride dissociation [9,20]. Therefore, evaluating the solution stability of Rubpy and Rubpe is essential before examining their interactions with biomacromolecules.

Both complexes were initially dissolved in minimal methanol and diluted to 60 μM in water, and their UV–Vis spectra were monitored for 6 h (Figure S4). No changes in the MLCT band positions were observed during this period, indicating that chloride substitution by water did not occur [21–23]. This invariance demonstrates that both complexes exhibit good stability in aqueous solution, supporting their suitability for biological studies in predominantly aqueous environments.

To further assess their solution behavior, UV–Vis spectra were recorded in PBS (pH 7.4) over 96 h. As shown in Figure 3, no shifts in the MLCT or intraligand absorption bands were detected for either complex. In similar Ru(II) polypyridyl systems, chloride substitution by water typically produces hypsochromic shifts in ca. 30 nm [21–23]; the absence of such changes confirms that Rubpy and Rubpe remain intact under physiological buffer conditions. This stability is consistent with literature reports describing slower substitution kinetics for Ru–Cl bonds trans to π-acceptor ligands, such as dmbpy, compared to those trans to strong σ-donors like primary amines [9,20].

Because proteins contain nucleophilic amino acid residues (e.g., –NH_2, –OH) capable of coordinating to metal centers, the stability of Rubpy and Rubpe in the presence of bovine serum albumin (BSA) was also evaluated (Figure S5). Similar to the results in PBS, no λ_{max} shifts were observed, indicating the absence of ligand exchange at Ru(II). A modest decrease in absorption intensity was detected, consistent with weak complex–protein association

rather than ligand substitution. This hypochromic effect supports the occurrence of non-covalent interactions with BSA, which were subsequently quantified using fluorescence spectroscopy, a more sensitive method for evaluating binding affinity.

Having established that both complexes remain structurally and spectroscopically stable in aqueous, physiological, and protein-containing environments, we proceeded to investigate their interactions with serum albumin and DNA, two key biomolecular targets involved in cellular transport, distribution, and molecular recognition.

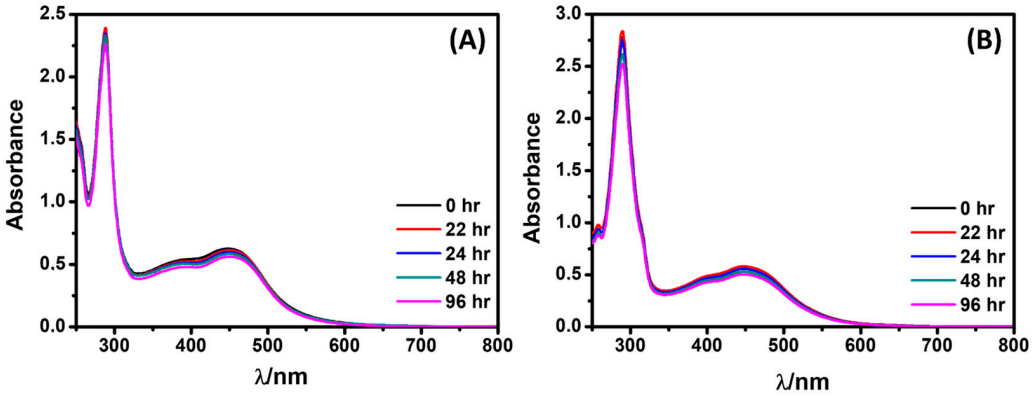


Figure 3. UV–Vis spectra of (**A**) Rubpy and (**B**) Rubpe in PBS buffer (pH 7.4) over a 96 h period. [Ru complex] = 60 μM, T = 25 °C.

2.2. Experimental Biomolecular Interactions

2.2.1. Interaction with Serum Albumin: Fluorescence Quenching and Binding Constants

Serum albumins represent the predominant protein fraction in blood plasma, accounting for around 60% of total protein and providing approximately 80% of blood osmotic pressure [24]. This biomolecule can bind reversibly to a variety of endogenous and exogenous molecules, such as drugs and other small bioactive compounds, playing an important role in drug transport [25]. Bovine serum albumin (BSA) is the most studied protein in biomimetic systems due to its structural homology with human serum albumin (HSA), with an identity of approximately 76% [26]. The primary structure of BSA consists of around 580 amino acids, including tryptophan and tyrosine residues, both fluorescent [27]. The fluorescence of bovine serum albumin is observed at 350 nm (λ_{ex} = 270 nm) primarily due to the emission of tryptophan, as the indole molar extinction coefficient of this residue is approximately five times greater than that of the phenyl group in the tyrosine residue [28]. Thus, the interaction between BSA and small molecules can modify the microenvironment surrounding the secondary structure of the protein chain, typically leading to a reduction in the fluorescence emitted by the intrinsic tryptophan group within this biomolecule [28].

As shown in Figure 4, an increase in the concentration of ruthenium complexes in the BSA solution systems causes a gradual decrease in the macromolecule's fluorescence intensity. This effect is associated with the quenching of the fluorophore's fluorescence. The observed quenching can be credited to changes in the tertiary structure of the protein, leading to alterations in the tryptophan environment of BSA and, therefore, indicating the binding of each complex to albumin [28]. There are two types of fluorescence quenching mechanisms: static and dynamic. In the former, a collision occurs between albumin and the ruthenium compound in the ground state, resulting in the formation of a non-fluorescent BSA–ruthenium complex. In the dynamic mechanism, the collision occurs between the fluorophore in the excited state and the ruthenium compound, forming a complex that returns to the ground state without emitting light. The efficiency of fluorescence quenching is related to the Stern–Volmer constant (K_{SV}) by the Stern-Volmer relation (Equation (1)), where F_0 is the fluorescence intensity in the absence of the quencher, F is the fluorescence

intensity in the presence of the quencher and [Q] is the concentration of the quencher, the ruthenium complexes.

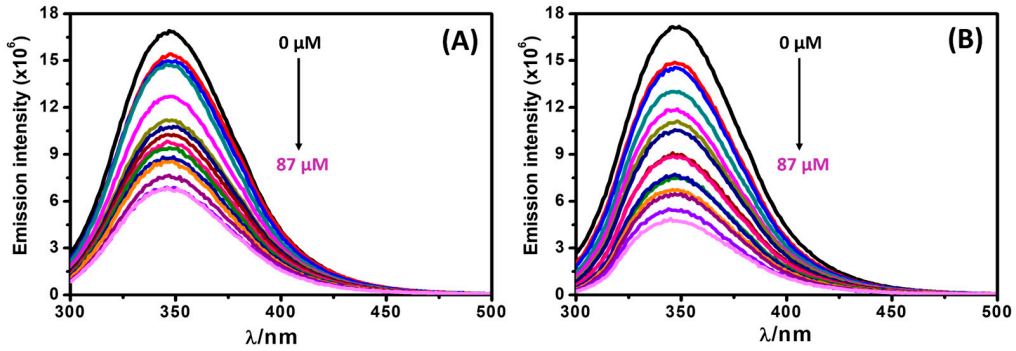


Figure 4. Steady-state fluorescence emission spectra for the interaction between BSA and (**A**) Rubpy and (**B**) Rubpe in PBS buffer (pH 7.4), at 25 °C. The complexes concentration ranged from 0 to 87 μM, and BSA presented fixed concentrations at 3 μM. λ_{exc} = 280 nm, excitation and emission slits of 5.0 nm and 1.0 nm, respectively.

Figure 5 displays a graph illustrating F_0/F as a function of the concentration of the ruthenium complexes. The data deviate from the linearity described by Equation (1), suggesting the presence of both static and dynamic quenching phenomena [9,25,28–30].

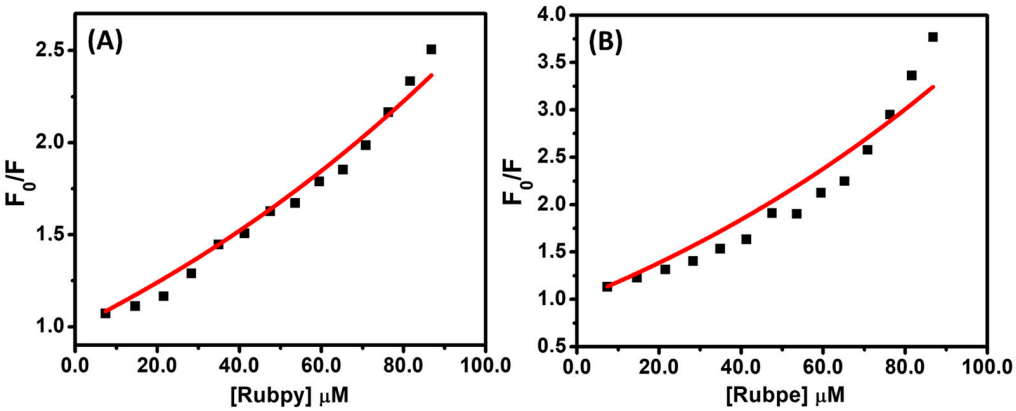


Figure 5. Stern-Volmer plots for the interaction (**A**) BSA-[Rubpy] and (**B**) BSA-[Rubpe].

In addition, the upward curve observed in Figure 5 is associated with a static component in the quenching mechanism. Therefore, a factor exp(V[Q]), where V is defined as the static quenching constant and is incorporated into the Stern–Volmer relationship (Equation (3)), to describe both quenching modes. The constant, *V* was determined from a plot of F_0/Fe^{V}[Q] versus [Q] and adjusting *V* until a linear plot was obtained (Figure S6). The highest correlation coefficient was used as the criterion for linearity to obtain a precise value of *V* [9]. The static quenching constant (V) for compounds was 5000 L mol^{-1} while the dynamic collisional quenching constant, K_{sv} was 0.61 × 10^5 M^{-1} for Rubpy and 1.27 × 10^5 M^{-1} for Rubpe (Table 1). Both complexes showed high values of the quenching constant indicating their great efficiency to interact strongly with BSA.

The values of the BSA-binding constant (K_b) and the number of binding sites per albumin (*n*) were calculated (Figure 6), and the results are shown in Table 1. For both complexes, the K_b value was around 10^5, indicating a strong interaction between the complex and the BSA protein [31]. Rubpy exhibited a slightly higher K_b value (2.89 × 10^5 M^{-1}) than Rubpe (1.97 × 10^5 M^{-1}), suggesting a marginally stronger interaction of Rubpy compared to Rubpe. The analysis of binding constants is highly useful for inferring how a molecular species will be distributed in blood plasma; the binding constant considered ideal falls

within the range of 10^4–10^6 L mol^{-1} [32]. Thus, the values obtained for Rubpy and Rubpe are sufficiently high for the compounds to bind to BSA for transport, but still low enough to allow their release from albumin upon reaching the target cells [9]. In addition, the number of quencher binding sites (*n*) calculated for both the [Rubpy]-BSA and [Rubpe]-BSA systems was approximately 1, indicating a single binding site for BSA for both complexes.

Table 1. Stern-Volmer (K_{sv}), binding constant (K_b) number of binding sites (*n*) of ruthenium(II) complexes to BSA (3 μM) in PBS, pH 7.4 at 25 °C. Data are represented as mean ± standard deviation of experiments performed in duplicate.

Complexes	K_{SV} ($\times 10^5$ M^{-1})	K_b ($\times 10^5$ M^{-1})	*n*
Rubpy	0.61 ± 0.02	2.89 ± 0.04	1.31
Rubpe	1.27 ± 0.08	1.97 ± 0.03	1.23

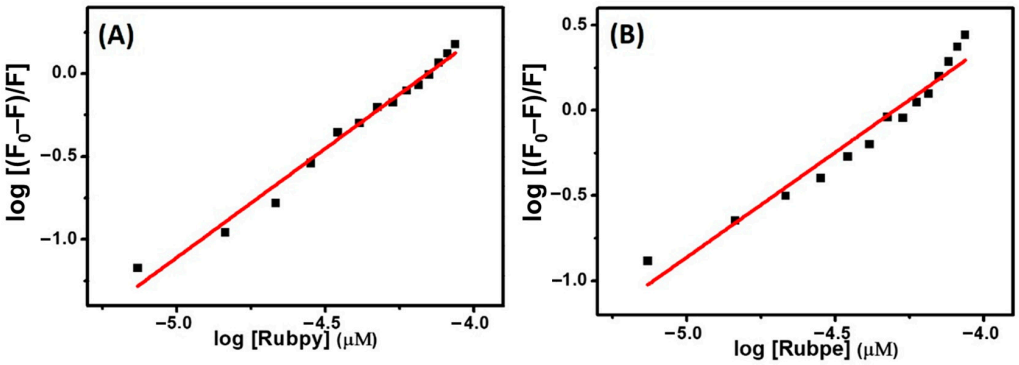


Figure 6. The plot of log [(F_0 − F/F] versus log [complex] for (**A**) Rubpy and (**B**) Rubpe.

2.2.2. DNA Interaction and Binding Constants (K_b) of Ruthenium Complexes

Beyond their interaction with albumin, which plays a central role in transport and pharmacokinetics, we also examined the interaction of the complexes with DNA, a key intracellular target for several metal-based therapeutics. Many clinically approved or clinically investigated anticancer agents act by binding to DNA and perturbing replication and transcription processes, making DNA–metal interactions a long-standing subject of interest in medicinal inorganic chemistry [33–35]. Such interactions may occur covalently, requiring a labile coordination site for metal–nucleobase binding, or non-covalently, through intercalation, groove binding, or electrostatic association with the negatively charged phosphate backbone [33–35].

The UV–Vis spectroscopy was employed to study [Ru-Complexe]-DNA interactions, the absorbance spectra of the ruthenium compounds in the presence of various concentrations of ss-DNA are shown in Figure S7. The ss-DNA biomolecule exhibited an absorption band (260 nm), while did not exhibit absorption in the MLCT band region [36]. As with the interaction of the complexes with BSA presented previously, no significant shift was observed in the λ_{max} of absorption values of the MLCT's bands for both complexes. The absence of MLCT band shift indicates that there is no exchange of coordinated ligands to the metal ruthenium(II) in the presence of ss-DNA. On the other hand, was observed a hyperchromic effect in MLCT's bands for both complexes (Figure S7A,B), this suggests that the electrostatic attraction or groove binding plays a dominant role, contributing to local destabilization of the DNA double helix [33–35]. In addition, the hypochromic effect (reduced absorbance) was associated with intercalating-type interactions arising from π-π-type stacking between ligands in the complex with the nitrogenous bases of DNA for many compounds [33–35]. To conclusively support that Rubpy and Rubpe complexes display an electrostatic interactions or interactions with the DNA groove, additional ex-

periments still would be needed, such as viscosity, thermal denaturation and/or circular dichroism [33–35]. Nevertheless, our research primarily focused on assessing the strength of the interaction between [Ru-Complex] and DNA by K_b rather than the mechanism of DNA interaction. Additionally, we employed ss-DNA as a model due to its reproducibility and well-defined optical signature in UV–Vis assays; however, we acknowledge that binding to double-stranded DNA may differ in magnitude or mode and warrants future biophysical analyses.

The intrinsic binding constant (Kb) was derived from the slope to the intercept obtained from the plot of $A_0/(A - A_0)$ versus 1/[DNA] (Figure S7C,D) and summarized in Table 2. Again, Rubpy complex showed the highest K_b value with DNA, corroborating previous data showing this compound has the highest interaction with BSA. The intrinsic binding constant is also an important indicator of the way of interaction of a metal complex with DNA. The K_b values for classical intercalators such as ethidium bromide (EB) and [Ru(phen)(dppz)] (phen = 1,10-phenanthroline; dppz = dipyrido[3,2-a:2′,3′-c]phenazine) are in the order of 10^6–10^7 M^{-1}, and smaller values were an indicator of electrostatic and partial intercalation type of mode of interaction, which are consistent with our previous hypothesis observed in the absorption spectrum of the complexes in the presence of DNA through the hyperchromic effect in the MLCT bands.

Table 2. Binding constant (Kb) of the interaction between Rubpy and Rubpe complexes and DNA. Values represent the mean ± standard error.

Complexes	K_b ($\times 10^3$ M^{-1})
Rubpy	1.47 ± 0.50
Rubpe	0.13 ± 0.03

Both complexes were studied as racemic mixtures, this approach is consistent with previous studies reporting similar binding constants for Δ/Λ enantiomers in Ru(II) polypyridyl systems [37–47]. Although chiral ruthenium polypyridyl complexes can interact differently with chiral biomolecules such as BSA, DNA, or RNA, numerous studies report that the two enantiomers often display binding constants within the same order of magnitude, with only minor differences between them [37–47]. Therefore, the use of racemic mixtures is not expected to significantly alter the interpretation of the binding affinities reported here.

The moderate K_b values obtained for both complexes suggest that DNA engagement is not the dominant contributor to cytotoxicity. To determine whether these interactions produce functional consequences at the DNA level, we next evaluated their capacity to induce plasmid cleavage under physiological conditions, described further below.

2.3. Computational Modeling of Biomolecular Binding

2.3.1. Docking to Serum Albumin: Structural Insights into Binding Sites I and II

While the experimental assays quantify binding strength in solution, docking studies were performed to visualize how Rubpy and Rubpe arrange within the BSA binding pockets and to identify the main non-covalent forces that stabilize these associations. This computational approach provides qualitative structural insight complementary to the fluorescence data.

Docking analysis confirmed that both complexes interact favorably with BSA, particularly within subdomain IIA, which contains the well-established Trp213 and Trp134 binding sites. For Rubpy, the lowest-energy pose at Trp213 (−8.18 kJ/mol; Figure 7) involved π–π T-shaped interactions with Trp213, hydrophobic contacts with Pro446, Cys447 and Lys439, and π–cation/π–anion contributions from Arg194 and Asp450. Additional stabilization was provided by amide–π interactions with Pro446 and Cys447. At the Trp134 pocket

(Figure 8), Rubpy also displayed a low-energy arrangement (−8.52 kJ/mol), driven by a hydrogen bond with Asn161, alkyl interactions with Leu283 and Pro281, π-alkyl contacts with Pro281 and Lys159, and π-anion contributions from Gln284.

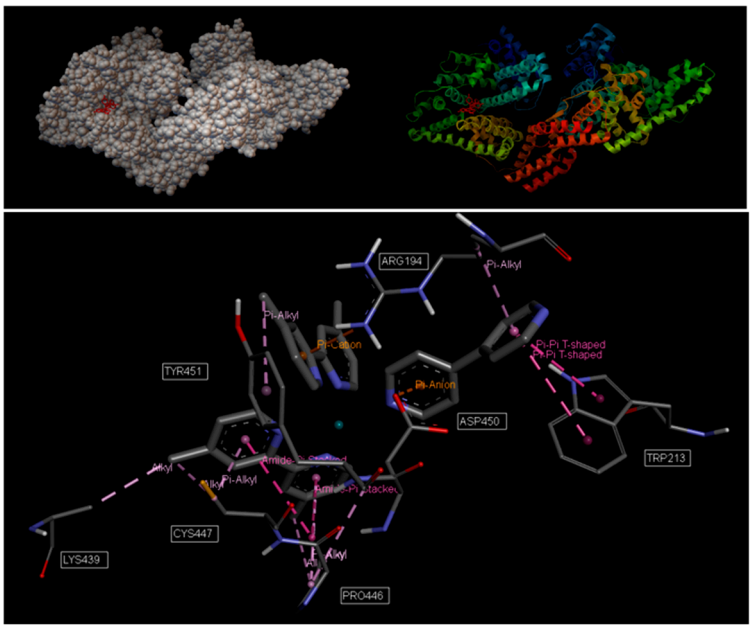


Figure 7. Molecular docking between the Rubpy complex and the tryptophan 213 site of BSA.

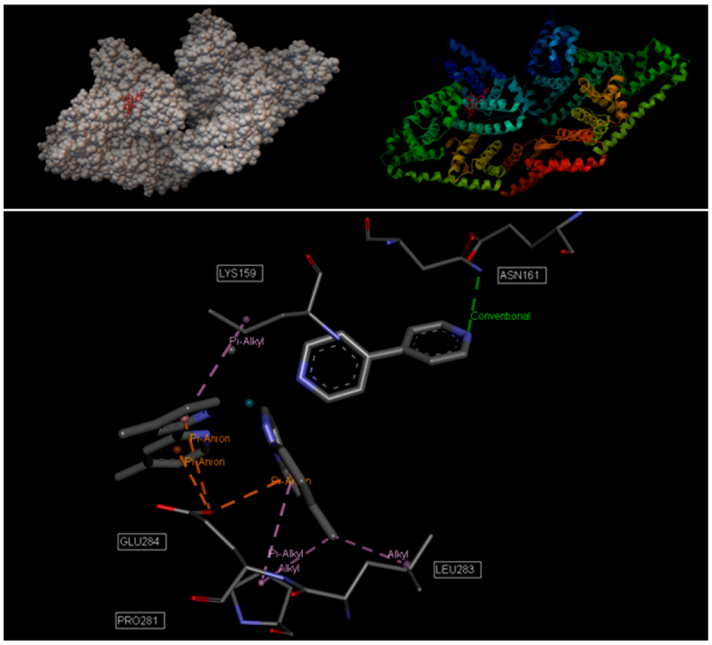


Figure 8. Molecular docking between the Rubpy complex and the tryptophan 134 site of BSA.

Rubpe exhibited a comparable interaction profile. At Trp213, its most stable configuration (−8.63 kJ/mol; Figure S8) was stabilized by alkyl, π-alkyl and π–σ interactions with Ala324, Arg208, Val215, Val234, Leu346, Lys350, Ala349 and Phe227. Amide–π contacts with Asp323 and Ala324, along with a hydrogen-bond–type interaction between a ligand nitrogen and the carbonyl oxygen of Leu346, further supported binding. A similarly favorable arrangement was obtained at the Trp134 pocket (−8.88 kJ/mol; Figure S9), dominated by π–π stacking with Trp134 and π-alkyl interactions with Lys131, Lys159, Tyr155 and Val163.

Overall, the docking results show that both Rubpy and Rubpe preferentially occupy the hydrophobic cavities of BSA subdomain IIA, engaging residues around Trp213 and Trp134 through aromatic, hydrophobic and electrostatic interactions. These structural models are consistent with the fluorescence quenching experiments, which measured the relative binding affinities under physiological conditions, while the docking simulations provide molecular-level insight into the spatial organization and types of interactions governing complex–protein association.

2.3.2. Docking to DNA: Predicted Binding Modes and Interaction Energies

Molecular docking simulations were used to investigate how Rubpy and Rubpe arrange within the DNA double helix and to identify the main stabilizing interactions governing association. Both complexes displayed a clear preference for the DNA minor groove.

For Rubpy, the lowest-energy pose (−7.8 kJ/mol; Figure 9) positioned the complex along the minor groove, stabilized primarily by a T-shaped π–π interaction with adenine 12 (chain A) and π-alkyl contacts with guanines 13 and 14 (chain B). These interactions were complemented by additional hydrophobic contributions involving the coordinated ligands. Rubpe exhibited a similar binding pattern, with its most stable configuration (−9.87 kJ/mol; Figure S10) also occupying the minor groove. Stabilization arose from π-alkyl interactions with thymine 9 and T-shaped π–π associations with thymine 9 and cytosine 6 of chain A. These results are consistent with general structure–binding principles, as compact aromatic ligands frequently accommodate the geometry of the minor groove, where π-based interactions with nucleobases are particularly favorable. The docking outcomes for Rubpy and Rubpe therefore reinforce the minor groove as the preferred region of interaction for both complexes.

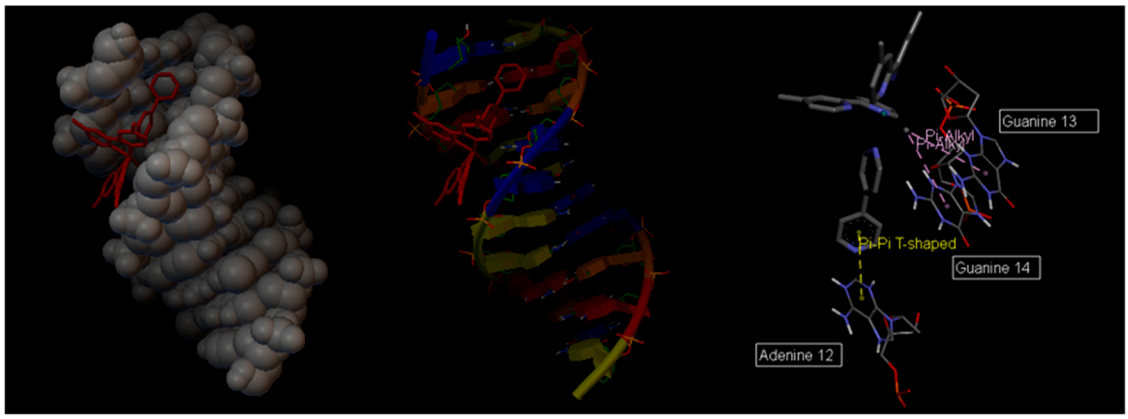


Figure 9. Molecular docking between the Rubpy complex and the macromolecule DNA.

Although docking suggested slightly stronger interactions for Rubpe, the experimental binding constants indicated the opposite trend, with Rubpy consistently showing higher affinity for DNA. This divergence is expected: docking evaluates geometric complementarity using rigid structures and simplified solvation models, whereas experimental measurements incorporate the full thermodynamic contributions of binding in solution, including solvent reorganization, ligand flexibility, hydrophobic effects and local structural rearrangements within DNA. In particular, the conformational flexibility and π-surface of the bpe ligand can artificially favor docking scores by enabling additional low-energy poses, even though these same features weaken π-stacking and reduce true binding affinity in solution. Thus, the docking preference for Rubpe reflects structural accommodation rather than actual thermodynamic stability. These structural considerations also help explain the experimental results: the π-conjugated bpy ligand in Rubpy promotes stronger π-stacking

and more stable non-covalent interactions with nucleobases, resulting in a higher intrinsic binding constant despite the slightly lower docking score. This behavior is fully consistent with previous reports showing that ligand planarity and π-surface are dominant contributors to the experimental DNA binding affinity of Ru(II) polypyridyl complexes. Highly planar, rigid ligands enhance π–π stacking and groove interactions, whereas non-planar or conformationally flexible ligands display significantly weaker binding despite favorable docking geometries [48,49]. Thus, while docking accurately identifies preferred binding geometries and interaction motifs, experimental affinities more faithfully reflect biologically relevant conditions [50]. The combined analysis therefore reconciles the apparent discrepancy and highlights how ligand rigidity and π-surface contribute differently to docking outcomes and experimental binding behaviors.

Together, the computational and spectroscopic analyses show that both complexes associate with DNA through non-covalent, minor-groove binding modes. To determine the functional consequences of these interactions, we next evaluated whether the complexes could induce structural alterations in DNA and how these molecular effects correlate with cellular uptake and cytotoxic responses.

2.4. Biological Consequences of DNA and Protein Interaction

2.4.1. DNA Cleavage Activity of Ruthenium Complexes

To further examine the functional consequences of complex–DNA association, plasmid cleavage assays were performed using pUC19 under physiological conditions. These tests complement the binding studies by assessing the ability of Rubpy and Rubpe to induce structural modifications in supercoiled DNA.

For Rubpy, concentrations of 50 and 100 μM promoted single-strand breaks (SSBs), with the extent of cleavage increasing at higher concentration (Figure 10). The electrophoretic profile revealed only Form I (supercoiled) and Form II (open circular), with no detectable linear Form III. Form II originates from SSBs that relax the helix, whereas Form III, observed only in the positive control containing restriction endonuclease, reflects double-strand breaks (DSBs) and migrates between the supercoiled and circular bands. These results indicate that Rubpy induces modest but detectable nuclease-like activity without generating DSBs.

A protective effect of DMSO was observed, consistent with partial quenching of reactive intermediates, whereas hydrogen peroxide did not significantly enhance DNA damage. This behavior suggests that cleavage proceeds mainly through structural destabilization or localized perturbation of the helix rather than through ROS-mediated oxidative pathways.

Rubpe displayed a similar concentration-dependent pattern (Figure S11), also limited to SSB formation and partially attenuated by DMSO, with no enhancement upon addition of hydrogen peroxide. These findings align with the spectroscopic Kb measurements: the moderate binding affinities observed for both complexes are sufficient to induce local unwinding of the double helix and facilitate single-strand scission. This is consistent with previous reports of Ru(II) polypyridyl complexes, where ligand electronic and steric properties modulate both DNA affinity and the extent of nuclease-like activity [51,52].

Overall, the cleavage data support a non-intercalative binding mode involving surface association accompanied by shallow groove interactions. Such interactions can destabilize the plasmid structure enough to promote SSBs but do not generate extensive or oxidative cleavage. These observations emphasize the key role of ligand environment in controlling DNA reactivity and motivate further mechanistic investigations into the specific interactions responsible for the observed nuclease-like behavior.

The absence of double-strand breaks and the modest level of single-strand scission indicate that DNA is not the primary cytotoxic target for these complexes, in agreement

with the dissociation observed between DNA affinity and antiproliferative potency. These findings suggest that the biological activity of Rubpy and Rubpe cannot be explained solely by their interactions with DNA. Because DNA cleavage requires intracellular availability of the complexes, we next evaluated their ability to enter cancer cells and accumulate at biologically relevant concentrations.

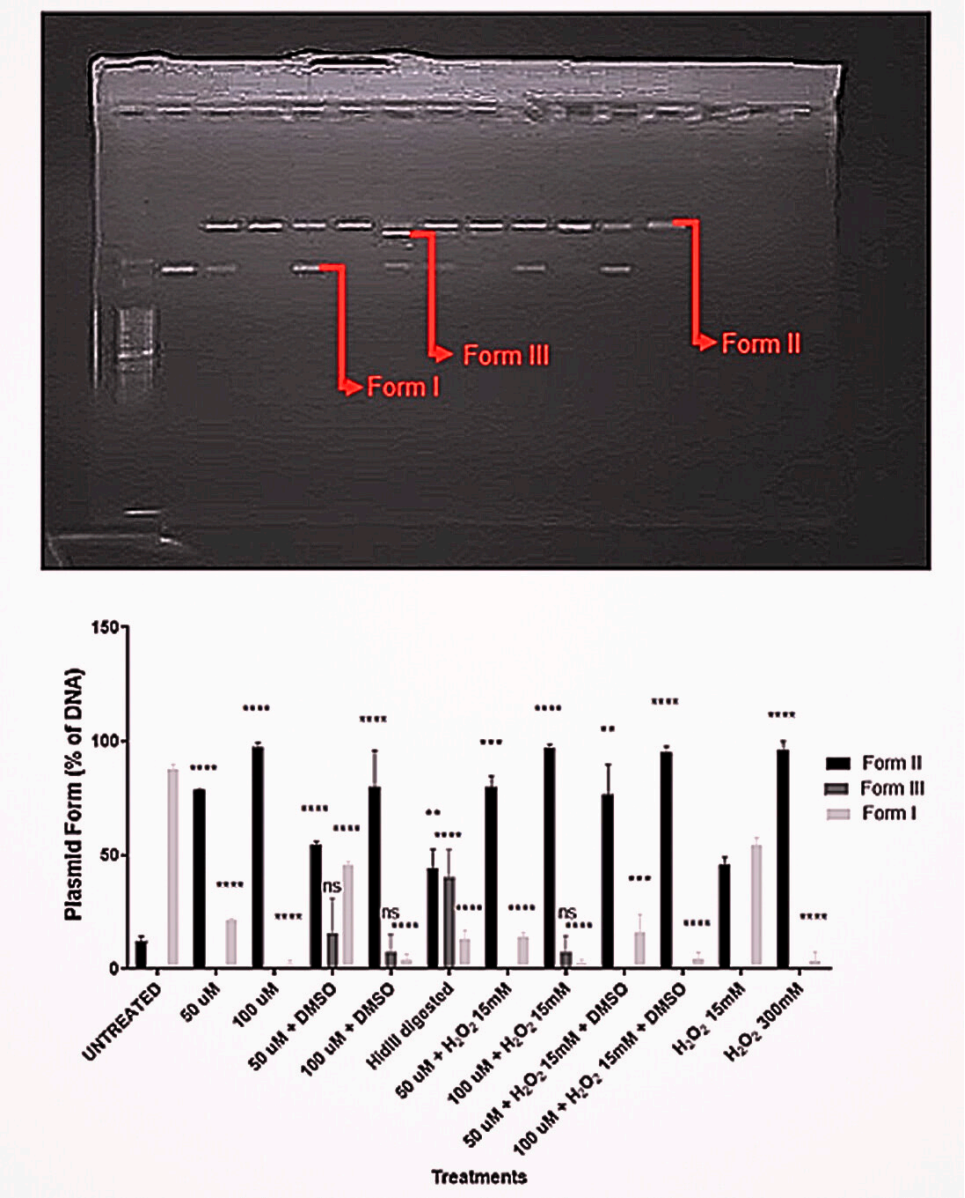


Figure 10. Image of plasmid degradation agarose gel and banding patterns found in each treatment, where 1: Marker; 2: Untreated control; 3: Rubpy (50 μM); 4: Rubpy (100 μM); 5: Rubpy (50 μM) + DMSO; 6: Rubpy (100 μM) + DMSO; 7: Hind III; 8: Rubpy (50 μM); 9: Rubpy (100 μM) + 15 mM H_2O_2; 10: Rubpy (50 μM) + 15 mM H_2O_2 + DMSO; 11: Rubpy (100 μM) + 15 mM H_2O_2 + DMSO; 12: 15 mM H_2O_2; 13: 300 mM H_2O_2. Graph representing the quantification of plasmid DNA in the bands found by agarose gel electrophoresis. Data expressed as the mean ± standard deviation of three assays. Statistical analysis was performed by 2-way ANOVA and multiple comparison by Bonferroni test * $p < 0.05$; ** $p < 0.01$; *** $p < 0.001$; **** $p < 0.0001$; ^{ns} not significant. Results were compared to the untreated control (in the absence of H_2O_2) and to the 15 mM H_2O_2 control (in the presence of H_2O_2).

2.4.2. Cellular Uptake in Cancer Cell Lines

The cellular uptake/incorporation properties of a molecule are critical for its application as a therapeutic agent. To exert cytotoxic effects, the compound must traverse the cell membrane, primarily composed of lipids and membrane proteins that regulate the passage of substances in and out of the cell [53]. Research on ruthenium complexes indicates that cellular uptake correlates directly with hydrophobicity, and higher cellular uptake leads to elevated cytotoxicity [54–58]. Thus, we exploited the cell uptake of ruthenium complexes into HeLa and MDA-MB-231 cells.

In HeLa cells, approximately 52% of Rubpy and around 47% of Rubpe were observed to incorporate (Figure 11). Meanwhile, the incorporation rates were 42% for Rubpy and 32% for Rubpe in MDA-MB-231 cells (Figure 11). Notably, the incorporation rates between Rubpy and Rubpe were very similar in both tested tumor cell lines. No significant difference in uptake percentages was observed between complexes in any of the examined tumor cell lines. The comparable uptake levels suggest that the structural modification in Rubpe, involving the insertion of a vinylene group (–CH=CH–), does not significantly alter the ability to permeate the cell membrane. This observation is consistent with the physicochemical similarity between the two complexes, including charge and size, which typically drive uptake via passive diffusion, facilitated diffusion, or endocytosis. The higher incorporation observed in HeLa cells compared to MDA-MB-231 cells may reflect differences in membrane composition or transport processes specific to each cell line.

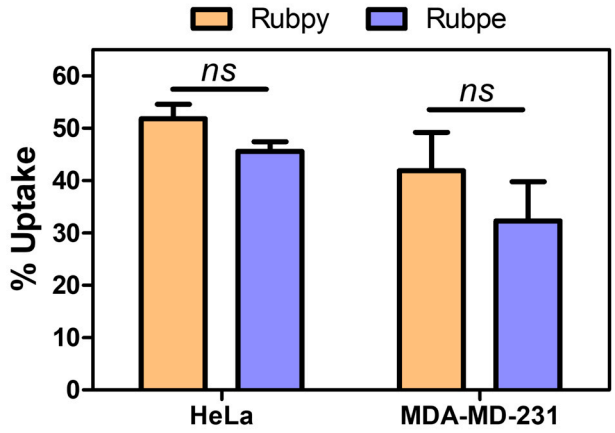


Figure 11. % Cellular uptake of Ru complexes (60 μM) incubated during 24 h in HeLa or MDA-MB-231 cells. Bars correspond to the mean ± standard deviation of three independent experiments with 4 replications in each experiment (n = 12), *ns* indicates that there is no statistical difference determined by the *Holm–Sidak* method, α= 0.05.

Ruthenium complexes can enter the cell through several mechanisms that include endocytosis and active transport (an energy-dependent process) or passive and facilitated (or energy-independent) diffusion [53]. These mechanisms generally depend on characteristics such as lipophilicity/hydrophilicity, charge, and size of the molecular structures. Given that the compounds share very similar structures, including their charges, it was expected that their cellular incorporation behaviors would yield comparable outcomes.

2.4.3. In Vitro Cytotoxicity Activity in HeLa and MDA-MB-231 Cells (MTT Assay)

To determine whether the molecular interactions observed in solution translate into biological activity, the cytotoxicity of Rubpy and Rubpe was evaluated in HeLa and MDA-MB-231 cells using the MTT assay after 24 h of incubation. This time was selected to minimize secondary metabolic effects often observed at longer exposures (48–72 h), enabling a clearer correlation with immediate molecular interactions. Both complexes reduced

cell viability in a dose-dependent manner (Figure 12), with Rubpe exhibiting consistently higher cytotoxicity than Rubpy in both cell lines.

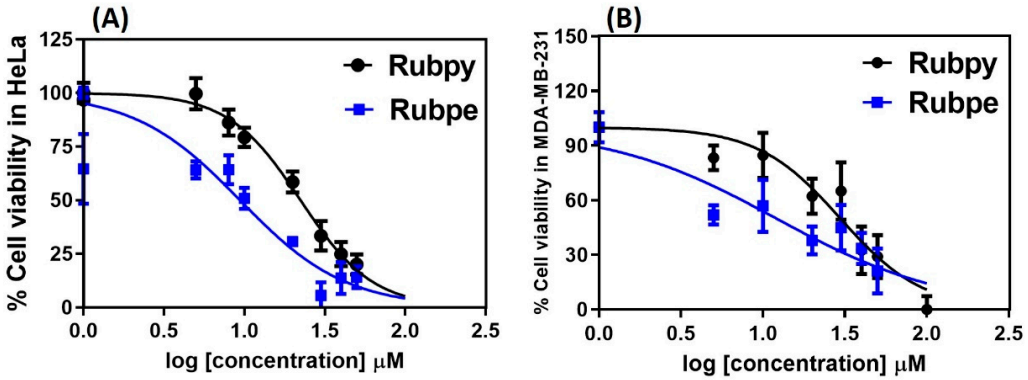


Figure 12. Dose–response curve on (**A**) HeLa cells and (**B**) MDA-MB-231 cells treated with Rubpy (black curves) and Rubpe (blue curves), during 24 h incubation under 5% CO_2 at 37 °C. Error bars represent the mean ± standard deviation of three independent experiments.

Rubpy displayed IC_{50} values of 22.37 μM (HeLa) and 29.69 μM (MDA-MB-231), whereas Rubpe showed IC_{50} values of 9.41 μM and 12.08 μM, respectively (Table 3). Thus, Rubpe was approximately 2.4-fold more potent than Rubpy in both models. These values fall well within the ranges reported for other ruthenium complexes acting on HeLa (13–200 μM) and MDA-MB-231 cells (5–72 μM) [59], confirming that both compounds exhibit comparatively strong cytotoxic effects [59].

Table 3. Cytotoxic effects expressed as IC_{50} values (μM) of the complexes $[Ru(dmbpy)_2Cl(bpy)](PF_6)$ and $[Ru(dmbpy)_2Cl(bpe)](PF_6)$, after 24 h treatment, toward two cancer cell lines, HeLa and MDA-MB-321.

Complexes	IC_{50} (μM)	
	HeLa	MDA-MB-231
Rubpy	22.37 ± 0.03	29.69 ± 0.06
Rubpe	9.41 ± 0.04	12.08 ± 0.10

To contextualize the cytotoxicity of Rubpy and Rubpe, their IC_{50} values against HeLa cells were compared with representative Ru(II) polypyridyl complexes reported in the literature under dark conditions (Table 4). HeLa cells were selected as the reference model because they are among the most frequently used human cancer cell lines in studies of Ru(II) polypyridyl complexes, allowing a more meaningful qualitative comparison across different reports. As summarized in Table 4, most Ru(II) polypyridyl complexes evaluated in HeLa cells exhibit IC_{50} values in the range of approximately 10–40 μM. Complexes containing extended planar ligands, such as phenanthroline- or dppz-based systems, typically display moderate cytotoxicity, with reported IC_{50} values between ~18 and 36 μM [60–62]. Similarly, Ru(II) complexes designed to target specific DNA motifs or transcriptional regulators show IC_{50} values in the low-to-mid micromolar range in HeLa cells [63,64].

Within this context, the IC_{50} values obtained for Rubpy (22.37 μM) and Rubpe (9.41 μM) fall well within, and in the case of Rubpe at the lower end of, the range reported for Ru(II) polypyridyl complexes in HeLa cells. Notably, Rubpe displays cytotoxicity comparable to or higher than several literature-reported Ru(II) complexes that incorporate more extended aromatic ligands or additional DNA-binding motifs, despite its comparatively simpler coordination environment. This observation highlights that subtle variations in ligand rigidity and π-surface can be sufficient to modulate cytotoxic responses in HeLa

cells, without the need for highly elaborate ligand frameworks. For comparison with a clinically established reference drug, cisplatin exhibits an IC_{50} value of 12.0 ± 0.52 μM in HeLa cells under comparable conditions [62]. Under the experimental conditions employed in this study, Rubpe shows cytotoxicity approaching that of cisplatin, whereas Rubpy is less potent but remains within the same order of magnitude. These results indicate that Rubpe, in particular, achieves cytotoxic efficacy in HeLa cells that is competitive with cisplatin.

Table 4. Cytotoxicity (IC_{50}) of some Ru(II) polypyridyl complexes and cisplatin in HeLa cells.

Complexes	IC_{50} (μM)	Ref.
Rubpy	22.37 ± 0.03	This work
Rubpe	9.41 ± 0.04	This work
$[Ru(phen)_2(tip)]^{2+}$	18.56 ± 0.67	[63]
$[Ru(phen)_2(bppp)]^{2+}$	32.0 ± 1.2	[61]
$[Ru(phen)_2(5\text{-idip})]^{2+}$	11.7 ± 1.2	[64]
$[Ru(phen)_2BrIPC]^{2+}$	18.15	[60]
$[Ru(phen)_2(dppz\text{-}7,8\text{-}(OMe)_2)]^{2+}$	36.5	[60]
Cisplatin	12.0 ± 0.52	[61]

phen: 1,10-phenantroline, tip: 2-thiophene-(1H-imidazo-4,5-f][1,10]phenanthroline, bppp = 11-bromo-pyrido[2′,3′:5,6]pyrazino[2,3-f][1,10]phenanthroline], 5-idip: 2-indole-[4,5-f][1,10]phenanthroline, BrIPC: 6-bromo-3-(1H-imidazo[4,5-f][1,10]-phenanthroline, dppz-7,8-$(OMe)_2$: 7,8-Dimethoxydipyrido[3,2-a:2′,3′-c]phenazine.

Notably, the IC_{50} values do not follow the same trend as the binding constants measured for BSA and DNA, where Rubpy exhibited slightly stronger affinity. This lack of correlation has been reported for other Ru complexes, where rapid aquation or strong protein binding does not necessarily predict cytotoxicity [59]. For instance, 4-amino-1,2,4-triazolium [trans-$RuCl_4$(4-amino-1,2,4-triazole)(dmso-S)] displays the fastest aquation and highest BSA affinity within its series but is also the least cytotoxic (IC_{50} = 621 μM in HT-29 cells) [59].

Cellular uptake is often associated with increased cytotoxicity [65–68]. However, Rubpy and Rubpe showed comparable internalization levels, approximately 52% and 47% in HeLa, and 42% and 32% in MDA-MB-231, respectively, suggesting that uptake alone does not account for the difference in antiproliferative activity. Furthermore, DNA binding and cleavage studies indicated that Rubpy interacts more strongly with DNA, yet Rubpe is the more cytotoxic compound, reinforcing the notion that DNA engagement is not the primary driver of activity for these complexes.

Although logP values were not experimentally determined, the increased flexibility and reduced π-surface of bpe relative to bpy are structural features that are known to modulate lipophilicity and membrane partition in Ru(II) polypyridyl systems. These characteristics can reduce π-stacking with DNA while favoring intracellular redistribution, which may contribute to the higher cytotoxicity observed for Rubpe [69,70]. We note that this interpretation is qualitative and is intended to provide a mechanistic context consistent with established structure–property trends in the literature [69,70]. The greater cytotoxic efficacy of Rubpe, despite its lower affinity for DNA and BSA, suggests contributions from additional biological pathways. In Ru(II) polypyridyl systems, mitochondrial accumulation, disruption of redox homeostasis and modulation of apoptotic signaling have frequently been reported as non-DNA mechanisms [5,13,65,71,72] and these processes may also be relevant here.

Beyond membrane partition, the conformational flexibility of the bpe ligand may facilitate dynamic ligand reorganization within the intracellular environment, enabling alternative interactions with proteins or organelles that are not accessible to the more rigid bpy analogue. Such behavior has been increasingly recognized in Ru(II) systems and may

contribute to the superior cytotoxicity observed for Rubpe. Further mechanistic studies will be required to clarify the intracellular pathways underlying these differences

Although the present study provides a controlled comparison between bpy- and bpe-containing Ru(II) complexes, some constraints should be acknowledged. ss-DNA was used as a spectroscopic model and may underestimate affinity relative to dsDNA; enantiomers were not separated; and mechanistic cellular pathways beyond DNA binding were not resolved. These limitations do not compromise the comparative trends but highlight opportunities for future refinement.

3. Materials and Methods

3.1. Materials

Analytical-grade reagents were used without purification in all experiments. The compounds *cis*-[Ru(dmbpy)$_2$Cl(bpy)](PF$_6$) and *cis*-[Ru(dmbpy)$_2$Cl(bpe)](PF$_6$) were prepared following the report by Toma and collaborators [73]. Product purity was confirmed by elemental analysis, mass spectrometry, and ^{1}H Nuclear Magnetic Resonance (NMR). Methanol, N,N′-dimethylformamide (DMF), dimethyl sulfoxide (DMSO), Bovine Serum Albumin (BSA), phosphate-buffered solution (PBS—10.0 mM phosphate buffer, 2.70 mM potassium chloride and 137 mM sodium chloride at pH 7.4), Dulbecco's Modified Eagle medium (DMEM) and 3-(4,5-dimethylthiazol-2-yl)-2,5-diphenyltetrazolium bromide (MTT) were purchased from Sigma-Aldrich (St. Louis, MO, USA).

3.2. Spectroscopic and Electrochemical Measurements

UV/Vis absorption spectra were achieved by using a Hewlett Packard 8453A diode array spectrophotometer (Palo Alto, CA, USA). Electrochemical measurements were recorded on an Autolab PGSTAT30 potentiostat (Eco-Chemie, Utrecht, The Netherlands) employing a standard three-electrode setup, with a platinum working electrode, a platinum wire auxiliary electrode, and a reference electrode consisting of Ag/AgNO$_3$ (10 mM; +0.503 V vs. NHE). Tetrabutylammonium perchlorate (Bu$_4$NClO$_4$; 0.10 M) was used as the electrolytes. UV/Vis absorption spectroelectrochemistry measurements were carried out using a custom-designed electrochemical cell equipped with a gold minigrid working electrode, an Ag/AgNO$_3$ (10 mM in acetonitrile) reference electrode, and a platinum wire auxiliary electrode mounted inside a quartz cuvette with a path length of 25 μm. The application of potentials was controlled by an EG&G PAR 173 potentiostat (Oak Ridge, TN, USA), and the spectra were recorded with an HP 8453A spectrophotometer. Steady-state emission measurements were carried out in a Horiba FluoroMax 4 spectrofluorimeter (Edison, NJ, USA). Samples were measured at 298 K in a 1.000 cm quartz cuvette with a closed cap. The solutions were derated with Ar before the measurements. Mass spectra were obtained on an Esquire 3000 Plus Bruker Daltonics Mass Spectrometer (Bremen, Germany), 4000 V capillary and 180 μL h^{-1} flow injection. Elemental Analyses were executed by using a Perkin Elmer 2400 series II analyzer (Waltham, MA, USA). The ^{1}H Nuclear Magnetic Resonance spectra were performed on a Bruker DRX 300 Spectrometer (Rheinstetten, Germany) using acetone-d_6 as solvent.

3.3. Studies of Complexes in Aqueous Solution

The stability of the complexes solutions was analyzed by UV–Vis spectroscopy recording the electronic spectra in water and in PBS buffer (pH 7.4). The final concentration of each complex was achieved by diluting small aliquots of freshly prepared concentrated methanolic stock solutions, 6×10^{-5} M. The resulting solutions were examined over 96 h at 25 °C.

It also evaluated the stability of the Rubpy and Rubpe complexes in the presence of bovine serum albumin (BSA). For that, the stock solution of the complex in methanol was evaporated using nitrogen gas to produce a film. Then, a solution of BSA in the PBS buffer (pH = 7.4) was added to the complex film. The final concentration of the ruthenium complex was 50 μM, and absorbance readings were taken as a function of time. The spectrum of BSA (3 μM) without complex was used to subtract from the spectra of the complex and BSA mixture solutions, better to visualize the overlap and similarity of the MLCT bands. The absorption spectra were recorded in a Shimadzu spectrophotometer model UV-2501 BC (Kyoto, Japan).

3.4. Molecular Docking Studies and Ligand Preparation

The ligands were developed employing Avogadro software version 1.1.1 and saved in mol2 format following structural optimization. Using the same software and its extensions tool, the structures were optimized based on the Universal Force Field (UFF). In AutoDock 1.5.7, ligand preparation involved adding polar hydrogen atoms, assigning Gasteiger charges, and removing potential water molecules.

Molecular docking simulation of ruthenium complexes were conducted using AutoDock 1.5.7 with DNA and BSA biomolecules. The crystal structures of DNA (126D) with the sequence CATGGCCATG (resolution: 2 Å) and BSA (3V03) (resolution: 2.7 Å) were retrieved from the Protein Data Bank (www.rcsb.org, accessed on 6 October 2025). Polar hydrogen atoms and Kollman charges were added to these structures, and water molecules surrounding the DNA/BSA were removed.

For blind docking, the DNA binding analysis used a grid box with dimensions 62 × 58 × 96 for the three complexes. BSA binding was assessed at two possible sites near tryptophan residues: tryptophan 134 (coordinates x = 45.989286, y = 36.667143, z = 25.500143) and tryptophan 213 (coordinates x = 101.169786, y = 28.225500, z = 19.778429), with a scan box size of 70 × 76 × 78.

Ligand-receptor binding calculations utilized the Lamarkian genetic algorithm, with 100 runs and 2.5 million evaluations. Visualization of DNA/BSA interactions was performed with Biovia Discovery Studio Visualizer version 2021.

3.5. Albumin Binding Studies

The study of protein binding was conducted through tryptophan fluorescence quenching experiments, employing bovine serum albumin (BSA) [28]. Quenching of the emission intensity of tryptophan residues of BSA at 350 nm was evaluated using the complexes Rubpy and Rubpe as quenchers. For that, the ruthenium complexes in different concentrations (0–87 μM) were added to a BSA (3 μM) solution in PBS (pH 7.4). Fluorescence spectra were collected in the range of 300–550 nm at an excitation wavelength of 280 nm, at 25 °C. All intrinsic quenching fluorescence experiments were executed in duplicate. The absorption spectra of the compounds in buffered solutions were recorded under the same experimental conditions, and to compensate for the inner filter effect [28], fluorescence intensity values were corrected for the absorbance of the individual complex using the Parker equation (Equation (1)) [74,75]:

$$F_{cor} = F_{obs} \times \frac{2,3dA_{exc}}{1-10^{-dA_{exc}}} \times 10^{gA_{em}} \times \frac{2,3sA_{em}}{1-10^{-sA_{em}}} \quad (1)$$

where F_{Cor} and F_{Obs} correspond to the corrected and observed fluorescence intensities, × respectively. A_{exc} and A_{em} denote the absorbances at the excitation λ_{exc} = 280 nm and λ_{em} = 350 nm, respectively. The optical path length of the cuvette (d) was 1.0 cm; "g" represents the distance between the edge of the excitation beam and "d" the edge of the cuvette (0.40 cm); and "s" is the excitation beam thickness (0.10 cm) [74–76].

The Stern-Vomer constant (K_{SV}) was calculated for ruthenium complexes from Stern-Volmer Equation (2) [28]:

$$\frac{F_0}{F} = 1 + K_{SV} \cdot [Q] \quad (2)$$

where F_0 and F represent the fluorescence intensities recorded in the absence and presence of the quencher, respectively. K_{sv} denotes the Stern–Volmer quenching constant, and [Q] corresponds to the concentration of the quencher.

The regular Stern–Volmer plots were not applicable for complexes Rubpy and Rubpe as the plot between F_0/F and [Q] displayed an upward curvature. An exponential term, $\exp^{(V[Q])}$, where V represents the static quenching constant, can be introduced into the Stern–Volmer equation (Equation (3)) to account for both quenching modes (static and dynamic) [9,29]:

$$F_0/F = (1 + K_{sv}[Q])e^{V[Q]} \quad (3)$$

The static quenching constant, V was determined by applying the equation and plotting $\{F_0/Fe^{V[Q]}\} - 1$ vs. [Q], systematically varying V until a linear relationship was observed. The optimal value of V was determined by identifying the plot that yielded the highest correlation coefficient. The dynamic (collisional) quenching constant, *Ksv*, was subsequently determined from the slope of the corresponding linear plots [9,29].

The strength of interaction between the compounds and BS) was determined by binding constant (K_b) obtained employing the modified Stern-Volmer (Equation (4)) below:

$$log\frac{(F_0 - F)}{F} = log\ K_b + n\ log\ [Q] \quad (4)$$

where F_0 and F are, respectively, the fluorescence intensity in the absence and presence of the quencher, K_b is the apparent binding constant of the quencher to the BSA, "*n*" is the number of binding sites of the quencher to the BSA and [Q] is the concentration of the quencher [28].

3.6. Cell Culture

The HeLa (human cervical cancer) cell line was obtained from Laboratory of Photoinduced Processes and Interfaces coordinated by Prof. Dr. Maurício Baptista (Institute of Chemistry, University of São Paulo, São Paulo—SP, Brazil). The MDA-MB-231 (human breast cancer) cell line was provided by the Laboratory of Nanobiotechnology Dr. Luiz Ricardo Goulart coordinated by Dr. Luciana Machado Bastos (Institute of Biotechnology, Federal University of Uberlandia, Uberlandia—Minas Gerais, Brazil).

HeLa (human cervical cancer) and MDA-MB-231 (human breast cancer) cell lines were cultivated as monolayer culture in Dulbecco's Modified Eagle Medium (DMEM) high glucose (4500 mg/L glucose, sodium pyruvate, L-glutamine, sodium bicarbonate and phenol red) supplemented with 10% fetal bovine serum (FBS), 100 UI/mL penicillin and 100 µg/mL streptomycin. The cells were kept at 37 °C, in an incubator with a 5% CO_2 atmosphere.

3.7. Cellular Uptake

HeLa or MDA-MB-231 cells (1.0×10^5 cell/well) were seeded in 1 mL of culture medium in 12-well plates and incubated at 37 °C and 5% CO_2 atmosphere during 24 h, for attachment of cells to the bottom of the well. After that, cells were treated with ruthenium complexes (60 µM) in 1 mL supplemented medium (DMEM with 10% FBS, 100 UI/mL penicillin and 100 µg/mL streptomycin) for 24 hours in the dark, 5% CO_2 at 37 °C. After this period, 500 µL of the supernatant solutions were removed from the well. The remaining cells in the well plate were washed with PBS, after which 500 µL of methanol was added to each well to extract the intracellularly incorporated complex. The percentage of cellular uptake was calculated as described previously [77,78]. Incubations

were performed in the dark to avoid uncontrolled photochemical processes that could induce ROS formation or alter Ru(II) electronic states, ensuring that all cytotoxic effects arose solely from ground-state interactions.

3.8. Cytotoxicity Activity (MTT Assay)

The cytotoxic activity of ruthenium complexes was analyzed by MTT assay [79–81]. For that, the cells (2.8×10^4 cells/well) were seeded in 300 µL of the medium in 48-well plates and incubated at 37 °C, in a 5% CO_2 atmosphere for 24 h. Next, the complexes were dissolved in methanol, which evaporated under argon flux, producing a film. Thus, the complex solutions were prepared by hydration of its film with supplemented culture medium (DMEM with 10% fetal bovine serum (FBS), 100 UI/mL penicillin and 100 µg/mL streptomycin). After 24 h of growth, cells were exposed to 300 µL of each concentration of complexes Rubpy or Rubpe (0, 1, 5, 8, 10, 20, 30, 40, 50 and 100 µM) for 24 h. Then, 100 µL of MTT (0.75 mg/mL in PBS, pH 7.4) solution was added to each well. After a further period of MTT incubation (3 h at 37 °C in 5% CO_2), the medium was removed, and the formazan crystals were solubilized by DMSO. The absorbance was registered using an automated microplate reader at 570 nm [79–81]. The percent of cell viability was calculated as Equation (5):

$$\%\ Cell\ viability\ = \frac{A_{treated(570\text{nm}-800\text{nm})}}{A_{control(570\text{nm}-800\text{nm})}} \times\ 100\% \quad (5)$$

where $A_{treated}$ is the Absorbance (in 570 nm–800 nm) of cells treated with ruthenium complexes and $A_{control}$ is the Absorbance (in 570 nm–800 nm) of control cells.

The IC_{50} values were determined by plotting the percentage viability vs. concentration on a logarithmic graph and fitting the dose–response curve with GraphPad Prism 5.0 Software.

3.9. DNA Interaction Assay by UV–Vis Spectroscopy

A stock solution of salmon sperm DNA (ss-DNA) was prepared by dissolving 5 mg of ss-DNA in 5 mL of PBS buffer (50 mM) containing 5 mM NaCl at pH 7.4. Prior to the experiments, DNA purity was verified by confirming an $Abs_{260nm}/Abs_{280nm} \geq 1.8$ The ss-DNA concentration was determined using the molar extinction coefficient at 260 nm $\varepsilon_{260} = 6600\ M^{-1}\ cm^{-1}$ [36]. The ss-DNA stock solution was maintained at 2–10 °C in an ice bath throughout the experiments. Solutions of Rubpy or Rubpe were prepared at a fixed concentration of 50 µM in PBS buffer (50 mM) containing NaCl (5 mM). Sequential additions of 10 µL aliquots of ss-DNA were then made, and after each addition the mixture was incubated for 5 min prior to recording the absorption spectra over an ss-DNA concentration range of 0–50 µM. The intrinsic binding constant (K_b) was derived from the slope/intercept relationship of th $A_0/(A - A_0)$ vs. 1/[DNA] according to the following Equation [36]

$$\frac{A_0}{A - A_0} = \frac{e_0}{e_{HG} - e_G} \times \frac{1}{K_b[DNA]} \quad (6)$$

3.10. DNA Cleavage Studies

To investigate the interaction of the complexes with DNA, we combined *cis*-[$Ru(dmbpy)_2Cl(bpy)$](PF_6) and *cis*-[$Ru(dmbpy)_2Cl(bpe)$](PF_6) with plasmid DNA from the pUC-19 vector (Lot. 1212425A, Clontech Laboratories, Inc., Takara Bio USA, Mountain View, CA, USA). The isolated plasmid was added to a series of 11 solutions, each with a total volume of 20 µL. Each solution contained 30 ng/µL of plasmid DNA treated with either 50 µM or 100 µM of *cis*-[$Ru(dmbpy)_2Cl(bpy)$](PF_6) or *cis*-[$Ru(dmbpy)_2Cl(bpe)$](PF_6) in PBS 1×, with or without dimethyl sulfoxide (DMSO, 0.05%), hydrogen peroxide (H_2O_2, 15 mM),

or a combination of both, as well as with H_2O_2 alone (300 mM). Controls included untreated plasmid DNA, plasmid DNA digested with the site-specific restriction enzyme Hind III, and plasmid DNA treated solely with H_2O_2. The reaction mixtures were incubated at 37 °C for 12 h, followed by the addition of 3 µL of loading buffer (0.25% bromophenol blue, 0.25% xylene cyanol, 30% glycerol, and 10 mM EDTA). Electrophoresis was then performed on a 0.8% agarose gel containing 0.05% ethidium bromide (10 µg/mL) in 0.5× TBE buffer (90 mM Tris-borate, pH 8.0, and 20 mM EDTA). The gels were run at 80 V for 3 h, and the resulting DNA bands were visualized under ultraviolet light and quantified using ImageJ software, version 1.53k (Java 1.8.0_172).

4. Conclusions

The two Ru(II) polypyridyl complexes, Rubpy and Rubpe, displayed closely related spectroscopic and redox properties, consistent with their structural similarity. Both complexes remained stable in aqueous solution and in the presence of BSA, ensuring that the species probed in biomolecular and cellular assays correspond to intact Ru(II) complexes. Fluorescence quenching experiments revealed binding constants on the order of 10^5 M^{-1}, indicating appreciable affinity toward serum albumin. UV–Vis titrations with ss-DNA showed hyperchromic MLCT responses and moderate intrinsic binding constants, with Rubpy exhibiting slightly higher affinity, consistent with a non-covalent interaction mode involving electrostatic and/or shallow groove association.

Cellular uptake levels were comparable for the two complexes in both HeLa and MDA-MB-231 cells. Nevertheless, Rubpe exhibited approximately 2.4-fold greater cytotoxicity than Rubpy, underscoring that neither uptake nor DNA binding alone accounts for the observed antiproliferative effects. This distinction suggests that additional intracellular pathways, beyond direct DNA involvement, likely contribute to the biological activity of Rubpe.

Overall, the integrated spectroscopic, computational, and cellular data highlight how subtle modifications in ligand rigidity and π-surface can modulate biomolecular interactions and cytotoxic responses in Ru(II) polypyridyl complexes, offering mechanistic insight that can guide future ligand design.

Supplementary Materials: The following supporting information can be downloaded at: https://www.mdpi.com/article/10.3390/inorganics14020063/s1, Figure S1. Spectroelectrochemical changes associated with the oxidation (A), the first (B) e second (C) reduction of Rubpy complex; Figure S2. Spectroelectrochemical changes associated with the oxidation following by reduction of Rubpy (A) and Rubpe (B) complexes; Figure S3. Spectroelectrochemical changes associated with the oxidation (A), the first (B) e second (C) reduction of Rubpe complex; Figure S4. UV–Vis spectra of (A) *cis*-$[RuCl(dmbpy)(bpy)]^+$ and (B) *cis*-$[RuCl(dmbpy)(bpe)]^+$ in 80% H_2O:20% MeOH over a period of 377 min. [Ru complex] = 60 µM, T = 25 °C; Figure S5. UV–Vis spectra of (A) *cis*-$[RuCl(dmbpy)(bpy)]^+$ and (B) *cis*-$[RuCl(dmbpy)(bpe)]^+$ in presence of 3 µM BSA. [Ru complex] = 50 µM, room temperature. Insert: MLCT band of complexes between 383 nm and 470 nm, highlighting hypochromic effect; Figure S6. Determination of the static suppression constant (V) using the Stern-Volmer equation; Figure S7. Absorption spectra of the *cis*-$[RuCl(dmbpy)(bpy)]^+$ (A) and *cis*-$[RuCl(dmbpy)(bpe)]^+$ (B) both at 50 µM, with successive additions of *ss*-DNA aliquots (ranging from 0 to 50 µM, in 50 mM PBS buffer containing 5 mM NaCl, pH 7.4) with 5 min of incubation at room temperature. Plots of $A_0/A\text{-}A_0$ versus 1/[DNA] derived to calculate K_b values of *cis*-$[RuCl(dmbpy)(bpy)]^+$ (C) and *cis*-$[RuCl(dmbpy)(bpe)]^+$ (D); Figure S8. Molecular docking between the Rubpe complex and the tryptophan 213 site of BSA; Figure S9. Molecular docking between the Rubpe complex and the tryptophan 134 site of BSA; Figure S10. Molecular docking between the Rubpe complex and the macromolecule DNA; Figure S11. Image of plasmid degradation agarose gel and banding patterns found in each treatment, where: 1: Marker;

2: Untreated control; 3: Rubpe (50 μM); 4: Rubpe (100 μM); 5: Rubpe (50 μM) + DMSO; 6: Rubpe (100 μM) + DMSO; 7: Hind III; 8: Rubpe (50 μM); 9: Rubpe (100 μM) + 15 mM H_2O_2; 10: Rubpe (50 μM) + 15 mM H_2O_2 + DMSO; 11: Rubpe (100 μM) + 15 mM H_2O_2 + DMSO; 12: 15 mM H_2O_2; 13: 300 mM H_2O_2. Graph representing the quantification of plasmid DNA in the bands found by agarose gel electrophoresis. Data expressed as the mean ± standard deviation of three assays. Statistical analysis was performed by 2-way ANOVA and multiple comparison by Bonferroni test * $p < 0.05$; ** $p < 0.01$; *** $p < 0.001$; **** $p < 0.0001$; ^{ns} not significant. Results were compared to the untreated control (in the absence of H_2O_2) and to the 15 mM H_2O_2 control (in the presence of H_2O_2).

Author Contributions: Investigation, formal analysis and validation, P.A.d.M., M.E.G.d.C., A.L.A.P., C.M.F.S. and R.C.L.; methodology, H.E.T., M.E.B., R.J.d.O.J., A.O.d.T.P., T.A.M. and T.M.T.; writing—original draft preparation, P.A.d.M., H.E.T., M.E.B., R.J.d.O.J., A.O.d.T.P., T.A.M. and T.M.T.; writing—review and editing, T.A.M. and T.M.T.; supervision, T.A.M. and T.M.T.; project administration, T.M.T.; funding acquisition, T.M.T. All authors have read and agreed to the published version of the manuscript.

Funding: This research was funded by *Fundação de Amparo à Pesquisa do Estado de Minas Gerais* (FAPEMIG, APQ-00704-21; APQ-02393-24; APQ-01044-21) and *Conselho Nacional de Desenvolvimento Científico e Tecnológico* (CNPq, 407282/2023-8; 308094/2025-5). This study was financed in part by *Coordenação de Aperfeiçoamento de Pessoal de Nível Superior* (CAPES—Finance Code 001 and PROEX).

Data Availability Statement: All data are contained within the manuscript. Raw data used for analysis will be shared upon request.

Acknowledgments: The authors acknowledge the financial support provided by FAPEMIG, CNPq and CAPES. Patrícia Alves de Matos thanks PhD scholarship grant from CAPES. Tayana M. Tsubone thanks the grant received by L'Oréal Brazil-UNESCO-ABC through "*For Women in Science*" Award 2023, in chemistry field.

Conflicts of Interest: The authors declare that they have no known competing financial interests or personal relationships that could have appeared to influence the work reported in this paper.

Abbreviations

The following abbreviations are used in this manuscript:

Rubpy	*cis*-[Ru(dmbpy)$_2$Cl(bpy)](PF$_6$)
Rubpe	*cis*-[Ru(dmbpy)$_2$Cl(bpe)](PF$_6$)
MLCT	metal-to-ligand charge transfer
BSA	bovine serum albumin

References

1. Kelland, L. The resurgence of platinum-based cancer chemotherapy. *Nat. Rev. Cancer* **2007**, *7*, 573–584. [CrossRef] [PubMed]
2. Thota, S.; Rodrigues, D.A.; Crans, D.C.; Barreiro, E.J. Ru(II) Compounds: Next-Generation Anticancer Metallotherapeutics? *J. Med. Chem.* **2018**, *61*, 5805–5821. [CrossRef] [PubMed]
3. Alessio, E. Thirty Years of the Drug Candidate NAMI-A and the Myths in the Field of Ruthenium Anticancer Compounds: A Personal Perspective. *Eur. J. Inorg. Chem.* **2016**, *2017*, 1549–1560. [CrossRef]
4. Bashir, M.; Mantoo, I.A.; Arjmand, F.; Tabassum, S.; Yousuf, I. An overview of advancement of organoruthenium (II) complexes as prospective anticancer agents. *Coord. Chem. Rev.* **2023**, *487*, 215169. [CrossRef]
5. Rilak Simović, A.; Masnikosa, R.; Bratsos, I.; Alessio, E. Chemistry and reactivity of ruthenium(II) complexes: DNA/protein binding mode and anticancer activity are related to the complex structure. *Coord. Chem. Rev.* **2019**, *398*, 113011. [CrossRef]
6. Baier, D.; Mendrina, T.; Schoenhacker-Alte, B.; Pirker, C.; Mohr, T.; Rusz, M.; Regner, B.; Schaier, M.; Sgarioto, N.; Raynal, N.J.; et al. The Lipid Metabolism as Target and Modulator of BOLD-100 Anticancer Activity: Crosstalk with Histone Acetylation. *Adv. Sci.* **2023**, *10*, e2301939. [CrossRef]
7. Skoczynska, A.; Lewinski, A.; Pokora, M.; Paneth, P.; Budzisz, E. An Overview of the Potential Medicinal and Pharmaceutical Properties of Ru(II)/(III) Complexes. *Int. J. Mol. Sci.* **2023**, *24*, 9512. [CrossRef]

8. Monro, S.; Colon, K.L.; Yin, H.; Roque, J., III; Konda, P.; Gujar, S.; Thummel, R.P.; Lilge, L.; Cameron, C.G.; McFarland, S.A. Transition Metal Complexes and Photodynamic Therapy from a Tumor-Centered Approach: Challenges, Opportunities, and Highlights from the Development of TLD1433. *Chem. Rev.* **2019**, *119*, 797–828. [CrossRef]
9. Milutinovic, M.M.; Rilak, A.; Bratsos, I.; Klisuric, O.; Vranes, M.; Gligorijevic, N.; Radulovic, S.; Bugarcic, Z.D. New 4′-(4-chlorophenyl)-2,2′:6′,2″-terpyridine ruthenium(II) complexes: Synthesis, characterization, interaction with DNA/BSA and cytotoxicity studies. *J. Inorg. Biochem.* **2017**, *169*, 1–12. [CrossRef]
10. Canovic, P.; Simovic, A.R.; Radisavljevic, S.; Bratsos, I.; Demitri, N.; Mitrovic, M.; Zelen, I.; Bugarcic, Z.D. Impact of aromaticity on anticancer activity of polypyridyl ruthenium(II) complexes: Synthesis, structure, DNA/protein binding, lipophilicity and anticancer activity. *JBIC J. Biol. Inorg. Chem.* **2017**, *22*, 1007–1028. [CrossRef] [PubMed]
11. Lazic, D.; Arsenijevic, A.; Puchta, R.; Bugarcic, Z.D.; Rilak, A. DNA binding properties, histidine interaction and cytotoxicity studies of water soluble ruthenium(ii) terpyridine complexes. *Dalton Trans.* **2016**, *45*, 4633–4646. [CrossRef]
12. Meng, X.; Leyva, M.L.; Jenny, M.; Gross, I.; Benosman, S.; Fricker, B.; Harlepp, S.; Hebraud, P.; Boos, A.; Wlosik, P.; et al. A ruthenium-containing organometallic compound reduces tumor growth through induction of the endoplasmic reticulum stress gene CHOP. *Cancer Res.* **2009**, *69*, 5458–5466. [CrossRef]
13. Huang, H.; Zhang, P.; Yu, B.; Chen, Y.; Wang, J.; Ji, L.; Chao, H. Targeting nucleus DNA with a cyclometalated dipyridophenazineruthenium(II) complex. *J. Med. Chem.* **2014**, *57*, 8971–8983. [CrossRef]
14. Khanvilkar, P.; Pulipaka, R.; Shirsath, K.; Devkar, R.; Chakraborty, D. Organometallic binuclear Ru(II) complexes: Design, synthesis, DNA/BSA binding interactions and in-vitro cytotoxicity against HeLa cell line. *Inorg. Chem. Commun.* **2019**, *102*, 134–140. [CrossRef]
15. Matos, C.P.; Valente, A.; Marques, F.; Adão, P.; Paula Robalo, M.; de Almeida, R.F.M.; Pessoa, J.C.; Santos, I.; Helena Garcia, M.; Tomaz, A.I. New polydentate Ru(III)-Salan complexes: Synthesis, characterization, anti-tumour activity and interaction with human serum proteins. *Inorganica Chim. Acta* **2013**, *394*, 616–626. [CrossRef]
16. Nehru, S.; Veeralakshmi, S.; Kalaiselvam, S.; Subin David, S.P.; Sandhya, J.; Arunachalam, S. Protein binding and antioxidant studies of diimine based emissive surfactant-ruthenium(II) complexes. *J. Biomol. Struct. Dyn.* **2021**, *39*, 1535–1546. [CrossRef]
17. Toma, S.H.; Uemi, M.; Nikolaou, S.; Tomazela, D.M.; Eberlin, M.N.; Toma, H.E. {trans-1, 4-Bis [(4-pyridyl) ethenyl] benzene}(2, 2′-bipyridine) ruthenium (II) Complexes and Their Supramolecular Assemblies with β-Cyclodextrin. *Inorg. Chem.* **2004**, *43*, 3521–3527. [CrossRef] [PubMed]
18. Meyer, T.J.; Huynh, M.H.V. The remarkable reactivity of high oxidation state ruthenium and osmium polypyridyl complexes. *Inorg. Chem.* **2003**, *42*, 8140–8160. [CrossRef] [PubMed]
19. Schafer, F.Q.; Buettner, G.R. Redox environment of the cell as viewed through the redox state of the glutathione disulfide/glutathione couple. *Free Radic. Biol. Med.* **2001**, *30*, 1191–1212. [CrossRef]
20. Rilak, A.; Bratsos, I.; Zangrando, E.; Kljun, J.; Turel, I.; Bugarcic, Z.D.; Alessio, E. New water-soluble ruthenium(II) terpyridine complexes for anticancer activity: Synthesis, characterization, activation kinetics, and interaction with guanine derivatives. *Inorg. Chem.* **2014**, *53*, 6113–6126. [CrossRef]
21. Matias, T.A.; Mangoni, A.P.; Toma, S.H.; Rein, F.N.; Rocha, R.C.; Toma, H.E.; Araki, K. Catalytic Water-Oxidation Activity of a Weakly Coupled Binuclear Ruthenium Polypyridyl Complex. *Eur. J. Inorg. Chem.* **2016**, *2016*, 5547–5556. [CrossRef]
22. Matias, T.A.; Rein, F.N.; Rocha, R.C.; Formiga, A.L.B.; Toma, H.E.; Araki, K. Effects of a strong pi-accepting ancillary ligand on the water oxidation activity of weakly coupled binuclear ruthenium catalysts. *Dalton Trans.* **2019**, *48*, 3009–3017. [CrossRef]
23. Matias, T.A.; Parussulo, A.L.A.; Benavides, P.A.; Guimarães, R.R.; Dourado, A.H.B.; Nakamura, M.; de Torresi, S.I.C.; Bertotti, M.; Araki, K. Polymeric binuclear ruthenium complex as efficient electrocatalyst for oxygen evolution reaction. *Electrochim. Acta* **2018**, *283*, 18–26. [CrossRef]
24. Sun, J.; Huang, Y.; Zheng, C.; Zhou, Y.; Liu, Y.; Liu, J. Ruthenium (II) complexes interact with human serum albumin and induce apoptosis of tumor cells. *Biol. Trace Elem. Res.* **2015**, *163*, 266–274. [CrossRef] [PubMed]
25. Htun, T. A negative deviation from Stern–Volmer equation in fluorescence quenching. *J. Fluoresc.* **2004**, *14*, 217–222. [CrossRef] [PubMed]
26. Kandagal, P.; Ashoka, S.; Seetharamappa, J.; Shaikh, S.; Jadegoud, Y.; Ijare, O.B. Study of the interaction of an anticancer drug with human and bovine serum albumin: Spectroscopic approach. *J. Pharm. Biomed. Anal.* **2006**, *41*, 393–399. [CrossRef]
27. Straight, R.; Spikes, J. Photosensitized oxidation of biomolecules. *Singlet O2* **1985**, *4*, 143.
28. Lakowicz, J.R. *Principles of Fluorescence Spectroscopy*; Springer: Boston, MA, US, 2006.
29. Seedher, N.; Agarwal, P. Complexation of fluoroquinolone antibiotics with human serum albumin: A fluorescence quenching study. *J. Lumin.* **2010**, *130*, 1841–1848. [CrossRef]
30. Eftink, M.R.; Ghiron, C.A. Fluorescence quenching studies with proteins. *Anal. Biochem.* **1981**, *114*, 199–227. [CrossRef]
31. B Neto, G.L.; Baptista, E.A.M.; Becca, G.H.S.; Nakatani, H.S.; Souza, V.R.D. Interações competitivas de complexos de rutênio contendo dimetilsulfóxido e ligantes N-heterocíclicos com albumina de soro humao. *Química Nova* **2020**, *43*, 261–270.

32. Lazniewska, J.; Agostino, M.; Hickey, S.M.; Parkinson-Lawrence, E.; Stagni, S.; Massi, M.; Brooks, D.A.; Plush, S.E. Spectroscopic and Molecular Docking Study of the Interaction between Neutral Re(I) Tetrazolate Complexes and Bovine Serum Albumin. *Chem. –A Eur. J.* **2021**, *27*, 11406–11417. [CrossRef]
33. Sirajuddin, M.; Ali, S.; Badshah, A. Drug-DNA interactions and their study by UV-Visible, fluorescence spectroscopies and cyclic voltametry. *J. Photochem. Photobiol. B Biol.* **2013**, *124*, 1–19. [CrossRef]
34. Rehman, S.U.; Sarwar, T.; Husain, M.A.; Ishqi, H.M.; Tabish, M. Studying non-covalent drug-DNA interactions. *Arch. Biochem. Biophys.* **2015**, *576*, 49–60. [CrossRef] [PubMed]
35. Kumar, N.; Kaushal, R.; Awasthi, P. Non-covalent binding studies of transition metal complexes with DNA: A review. *J. Mol. Struct.* **2023**, *1288*, 135751. [CrossRef]
36. de Lavor, T.S.; Teixeira, M.H.S.; de Matos, P.A.; Lino, R.C.; Silva, C.M.F.; do Carmo, M.E.G.; Beletti, M.E.; Patrocinio, A.O.T.; de Oliveira Junior, R.J.; Tsubone, T.M. The impact of biomolecule interactions on the cytotoxic effects of rhenium(I) tricarbonyl complexes. *J. Inorg. Biochem.* **2024**, *257*, 112600. [CrossRef] [PubMed]
37. Zhang, P.; Wang, J.; Huang, H.; Qiao, L.; Ji, L.; Chao, H. Chiral ruthenium(II) complexes with phenolic hydroxyl groups as dual poisons of topoisomerases I and IIalpha. *Dalton Trans.* **2013**, *42*, 8907–8917. [CrossRef]
38. Sun, D.; Liu, Y.; Liu, D.; Zhang, R.; Yang, X.; Liu, J. Stabilization of G-quadruplex DNA, inhibition of telomerase activity and live cell imaging studies of chiral ruthenium(II) complexes. *Chem. –A Eur. J.* **2012**, *18*, 4285–4295. [CrossRef]
39. Nie, Y.; Dai, Z.; Fozia; Zhao, G.; Jiang, J.; Xu, X.; Ying, M.; Wang, Y.; Hu, Z.; Xu, H. Comparative studies on DNA-binding mechanisms between enantiomers of a polypyridyl ruthenium (II) complex. *J. Phys. Chem. B* **2022**, *126*, 4787–4798. [CrossRef]
40. Zou, S.; Li, G.; Rees, T.W.; Jin, C.; Huang, J.; Chen, Y.; Ji, L.; Chao, H. Interfering with DNA High-Order Structures using Chiral Ruthenium(II) Complexes. *Chem. –A Eur. J.* **2018**, *24*, 690–698. [CrossRef]
41. Wang, Y.C.; Qian, C.; Peng, Z.L.; Hou, X.J.; Wang, L.L.; Chao, H.; Ji, L.N. Dual topoisomerase I and II poisoning by chiral Ru(II) complexes containing 2-thiophenylimidazo[4,5-f][1,10]phenanthroline derivatives. *J. Inorg. Biochem.* **2014**, *130*, 15–27. [CrossRef]
42. Dong, Z.; Liu, X.; Tan, L. Biophysical insights into the interaction of two enantiomers of Ru (II) complex [Ru (bpy) 2 (7-CH 3-dppz)] 2+ with the RNA poly (UA∗ U) triplex. *JBIC J. Biol. Inorg. Chem.* **2020**, *25*, 1085–1095. [CrossRef]
43. Gao, F.; Chao, H.; Wang, J.Q.; Yuan, Y.X.; Sun, B.; Wei, Y.F.; Peng, B.; Ji, L.N. Targeting topoisomerase II with the chiral DNA-intercalating ruthenium(II) polypyridyl complexes. *JBIC J. Biol. Inorg. Chem.* **2007**, *12*, 1015–1027. [CrossRef] [PubMed]
44. Jiang, L.; Liu, X.; Tan, L. Synthesis and characterization of chiral Ru(II) polypyridyl complexes and their binding and stabilizing effects toward triple-helical RNA. *J. Inorg. Biochem.* **2020**, *213*, 111263. [CrossRef]
45. Wang, J.Q.; Zhang, P.Y.; Qian, C.; Hou, X.J.; Ji, L.N.; Chao, H. Mitochondria are the primary target in the induction of apoptosis by chiral ruthenium(II) polypyridyl complexes in cancer cells. *JBIC J. Biol. Inorg. Chem.* **2014**, *19*, 335–348. [CrossRef]
46. Yuan, F.; Chen, X.; Liu, Y.; Zhang, T.; Sun, D.; Liu, J. Chiral ruthenium complexes induce apoptosis of tumor cell and interact with bovine serum albumin. *Chirality* **2012**, *24*, 174–180. [CrossRef]
47. Wen, B.; Liu, X.; Tan, L. Binding and stabilizating effect of RNA triplex poly(U)·poly(A)*poly(U) by enantiomers of ruthenium(II) polypyridyl complex $[Ru(bpy)_2(dppx)]^{2+}$. *J. Biol. Inorg. Chem.* **2023**, *28*, 509–517. [CrossRef]
48. Xu, H.; Zheng, K.-C.; Chen, Y.; Li, Y.-Z.; Lin, L.-J.; Li, H.; Zhang, P.-X.; Ji, L.-N. Effects of ligand planarity on the interaction of polypyridyl Ru (II) complexes with DNA. *Dalton Trans.* **2003**, *11*, 2260–2268. [CrossRef]
49. Zhen, Q.-X.; Ye, B.-H.; Zhang, Q.-L.; Liu, J.-G.; Li, H.; Ji, L.-N.; Wang, L. Synthesis, characterization and the effect of ligand planarity of $[Ru(bpy)_2L]^{2+}$ on DNA binding affinity. *J. Inorg. Biochem.* **1999**, *76*, 47–53. [CrossRef]
50. Kitchen, D.B.; Decornez, H.; Furr, J.R.; Bajorath, J. Docking and scoring in virtual screening for drug discovery: Methods and applications. *Nat. Rev. Drug Discov.* **2004**, *3*, 935–949. [CrossRef] [PubMed]
51. Hu, X.; Liu, N.Y.; Deng, Y.Q.; Wang, S.; Liu, T.; Liu, X.W. Photoinduced DNA Cleavage and Photocytotoxic of Phenanthroline-Based Ligand Ruthenium Compounds. *Molecules* **2021**, *26*, 3471. [CrossRef] [PubMed]
52. Sangeetha, S.; Murali, M. Cytotoxic Ruthenium(II) Complexes Containing a Dangling Pyridine: Selectivity for Diseased Cells Mediated by pH-Dependent DNA Binding. *Inorg. Chem.* **2022**, *61*, 2864–2882. [CrossRef]
53. Sudhindra, P.; Ajay Sharma, S.; Roy, N.; Moharana, P.; Paira, P. Recent advances in cytotoxicity, cellular uptake and mechanism of action of ruthenium metallodrugs: A review. *Polyhedron* **2020**, *192*, 114827. [CrossRef]
54. Chen, L.M.; Peng, F.; Li, G.D.; Jie, X.M.; Cai, K.R.; Cai, C.; Zhong, Y.; Zeng, H.; Li, W.; Zhang, Z.; et al. he studies on the cytotoxicity in vitro, cellular uptake, cell cycle arrest and apoptosis-inducing properties of ruthenium methylimidazole complex $[Ru(MeIm)_4(p\text{-}cpip)]^{2+}$. *J. Inorg. Biochem.* **2016**, *156*, 64–74. [CrossRef] [PubMed]
55. Mehanna, S.; Mansour, N.; Audi, H.; Bodman-Smith, K.; Mroueh, M.A.; Taleb, R.I.; Daher, C.F.; Khnayzer, R.S. Enhanced cellular uptake and photochemotherapeutic potential of a lipophilic strained Ru(ii) polypyridyl complex. *RSC Adv.* **2019**, *9*, 17254–17265. [CrossRef] [PubMed]
56. Piccolo, M.; Misso, G.; Ferraro, M.G.; Riccardi, C.; Capuozzo, A.; Zarone, M.R.; Maione, F.; Trifuoggi, M.; Stiuso, P.; D'Errico, G.; et al. Exploring cellular uptake, accumulation and mechanism of action of a cationic Ru-based nanosystem in human preclinical models of breast cancer. *Sci. Rep.* **2019**, *9*, 7006. [CrossRef]

57. Tan, C.; Lai, S.; Wu, S.; Hu, S.; Zhou, L.; Chen, Y.; Wang, M.; Zhu, Y.; Lian, W.; Peng, W.; et al. Nuclear permeable ruthenium(II) beta-carboline complexes induce autophagy to antagonize mitochondrial-mediated apoptosis. *J. Med. Chem.* **2010**, *53*, 7613–7624. [CrossRef] [PubMed]
58. Zhang, S.Q.; Meng, T.T.; Li, J.; Hong, F.; Liu, J.; Wang, Y.; Gao, L.H.; Zhao, H.; Wang, K.Z. Near-IR/Visible-Emitting Thiophenyl-Based Ru(II) Complexes: Efficient Photodynamic Therapy, Cellular Uptake, and DNA Binding. *Inorg. Chem.* **2019**, *58*, 14244–14259. [CrossRef]
59. Omondi, R.O.; Ojwach, S.O.; Jaganyi, D. Review of comparative studies of cytotoxic activities of Pt(II), Pd(II), Ru(II)/(III) and Au(III) complexes, their kinetics of ligand substitution reactions and DNA/BSA interactions. *Inorganica Chim. Acta* **2020**, *512*, 119883. [CrossRef]
60. Hess, J.; Huang, H.; Kaiser, A.; Pierroz, V.; Blacque, O.; Chao, H.; Gasser, G. Evaluation of the medicinal potential of two ruthenium (II) polypyridine complexes as one-and two-photon photodynamic therapy photosensitizers. *Chem. –A Eur. J.* **2017**, *23*, 9888–9896. [CrossRef]
61. Srishailam, A.; Gabra, N.M.; Kumar, Y.P.; Reddy, K.L.; Devi, C.S.; Kumar, D.A.; Singh, S.S.; Satyanarayana, S. Synthesis, characterization; DNA binding and antitumor activity of ruthenium (II) polypyridyl complexes. *J. Photochem. Photobiol. B Biol.* **2014**, *141*, 47–58. [CrossRef]
62. Deepika, N.; Devi, C.S.; Kumar, Y.P.; Reddy, K.L.; Reddy, P.V.; Kumar, D.A.; Singh, S.S.; Satyanarayana, S. DNA-binding, cytotoxicity, cellular uptake, apoptosis and photocleavage studies of Ru (II) complexes. *J. Photochem. Photobiol. B Biol.* **2016**, *160*, 142–153. [CrossRef]
63. Wang, C.; Yu, Q.; Yang, L.; Liu, Y.; Sun, D.; Huang, Y.; Zhou, Y.; Zhang, Q.; Liu, J. Ruthenium (II) polypyridyl complexes stabilize the bcl-2 promoter quadruplex and induce apoptosis of Hela tumor cells. *Biometals* **2013**, *26*, 387–402. [CrossRef]
64. Yu, Q.; Liu, Y.; Xu, L.; Zheng, C.; Le, F.; Qin, X.; Liu, Y.; Liu, J. Ruthenium (II) polypyridyl complexes: Cellular uptake, cell image and apoptosis of HeLa cancer cells induced by double targets. *Eur. J. Med. Chem.* **2014**, *82*, 82–95. [CrossRef]
65. Zeng, L.; Chen, Y.; Huang, H.; Wang, J.; Zhao, D.; Ji, L.; Chao, H. Cyclometalated Ruthenium(II) Anthraquinone Complexes Exhibit Strong Anticancer Activity in Hypoxic Tumor Cells. *Chem. –A Eur. J.* **2015**, *21*, 15308–15319. [CrossRef]
66. Erenburg, S.B.; Trubina, S.V.; Yukhin, Y.M.; Sharafutdinov, M.R. Structural characteristics of amorphous K-Bi citrate (De-Nol) and its aqueous solutions from EXAFS spectra. *J. Inorg. Biochem.* **2017**, *166*, 94–99. [CrossRef]
67. Mendoza-Ferri, M.G.; Hartinger, C.G.; Mendoza, M.A.; Groessl, M.; Egger, A.E.; Eichinger, R.E.; Mangrum, J.B.; Farrell, N.P.; Maruszak, M.; Bednarski, P.J.; et al. Transferring the concept of multinuclearity to ruthenium complexes for improvement of anticancer activity. *J. Med. Chem.* **2009**, *52*, 916–925. [CrossRef]
68. Giannini, F.; Paul, L.E.H.; Furrer, J.; Therrien, B.; Süss-Fink, G. Highly cytotoxic diruthenium trithiolato complexes of the type $[(\eta^6\text{-p-MeC}_6\text{H}_4\text{Pri})_2\text{Ru}_2(\mu_2\text{-SR})_3]$+: Synthesis, characterization, molecular structure and in vitro anticancer activity. *New J. Chem.* **2013**, *37*, 3503–3511. [CrossRef]
69. Conti, L.; Macedi, E.; Giorgi, C.; Valtancoli, B.; Fusi, V. Combination of light and Ru (II) polypyridyl complexes: Recent advances in the development of new anticancer drugs. *Coord. Chem. Rev.* **2022**, *469*, 214656. [CrossRef]
70. Zeng, L.; Gupta, P.; Chen, Y.; Wang, E.; Ji, L.; Chao, H.; Chen, Z.-S. The development of anticancer ruthenium (II) complexes: From single molecule compounds to nanomaterials. *Chem. Soc. Rev.* **2017**, *46*, 5771–5804. [CrossRef] [PubMed]
71. Wang, J.-Q.; Zhao, Z.-Z.; Bo, H.-B.; Chen, Q.-Z. Synthesis, characterization, and antitumor properties of ruthenium(II) anthraquinone complexes. *J. Coord. Chem.* **2016**, *69*, 177–189. [CrossRef]
72. Li, G.; Sun, L.; Ji, L.; Chao, H. Ruthenium(ii) complexes with dppz: From molecular photoswitch to biological applications. *Dalton Trans.* **2016**, *45*, 13261–13276. [CrossRef]
73. Parussulo, A.L.A.; Matias, T.A.; Guimaraes, R.R.; Toma, S.H.; Araki, K.; Toma, H.E. Accessing the charge separation effects in dye-sensitized solar cells based on a vectorial planning of supramolecular ruthenium dyes. *Inorganica Chim. Acta* **2016**, *453*, 764–770. [CrossRef]
74. Parker, C.; Barnes, W. Some experiments with spectrofluorimeters and filter fluorimeters. *Analyst* **1957**, *82*, 606–618. [CrossRef]
75. Kumar Panigrahi, S.; Kumar Mishra, A. Inner filter effect in fluorescence spectroscopy: As a problem and as a solution. *J. Photochem. Photobiol. C Photochem. Rev.* **2019**, *41*, 100318. [CrossRef]
76. MacDonald, B.C.; Lvin, S.J.; Patterson, H. Correction of fluorescence inner filter effects and the partitioning of pyrene to dissolved organic carbon. *Anal. Chim. Acta* **1997**, *338*, 155–162. [CrossRef]
77. do Carmo, M.E.G.; de Matos, P.A.; Maia, P.I.S.; Machado, A.E.H.; Beletti, M.E.; Tsubone, T.M.; Patrocinio, A.O.T. The photophysics of Ir(III) cyclometalated complexes containing the 2-(2-pyridyl)benzimidazole ancillary ligand: Protonation effect and their potential as specific lysosome probes in cells. *J. Photochem. Photobiol. A Chem.* **2024**, *448*, 115339. [CrossRef]
78. Tsubone, T.M.; Martins, W.K.; Pavani, C.; Junqueira, H.C.; Itri, R.; Baptista, M.S. Enhanced efficiency of cell death by lysosome-specific photodamage. *Sci. Rep.* **2017**, *7*, 6734. [CrossRef]
79. Mosmann, T. Rapid colorimetric assay for cellular growth and survival: Application to proliferation and cytotoxicity assays. *J. Immunol. Methods* **1983**, *65*, 55–63. [CrossRef]

80. Riss, T.; Niles, A.; Minor, L. Cell viability assays assay guidance manual. In *Assay Guide Manual*; Eli Lilly & Company: Bethesda, MD, USA, 2004.
81. *ISO 10993-5:2009*; Biological Evaluation of Medical Devices—Part 5: Tests for In Vitro Cytotoxicity Standardization. International Organization for Standardization: Geneva, Switzerland, 2009.

Disclaimer/Publisher's Note: The statements, opinions and data contained in all publications are solely those of the individual author(s) and contributor(s) and not of MDPI and/or the editor(s). MDPI and/or the editor(s) disclaim responsibility for any injury to people or property resulting from any ideas, methods, instructions or products referred to in the content.